The Influence of In-Medium Modifications on Quasi-Elastic Electron and Neutrino Scattering on Nuclei

David F. Kalok

Giessen den 13.06.2007

Diplomarbeit

Justus-Liebig-Universität Gießen
Institut für Theoretische Physik

There is a theory which states that if anybody ever discovers exactly what the Universe is for and why it is here, it will instantly disappear and be replaced by something even more bizarre and inexplicable. There is another theory which states that this has already happened.

Douglas Adams: The Hitchhiker's Guide to the Galaxy

Contents

1 Introduction

Since the 1950's electron-nucleus scattering experiments have been performed that opened up a new era of nuclear structure investigations [BGPR96]. In 1955, Hofstadter and Mc Allister observed the finite size of a proton by deviations from the Rosenbluth cross section for elastic electron scattering. The intrinsic structure of the neutron was first probed by Havens et al. and Fermi and Marshall in the year 1947. It was shown by Foldy in the years 1951-1952 that the anomalous magnetic moment, suggested by Pauli in 1941, plays a role in electron neutron interaction.

More than 50 years of electron nucleus scattering experiments have shown that it is probably the best method to investigate nuclei and their constituents [BGPR96]. For light nuclei and high energy electrons the Born approximation, i.e. one photon exchange between electron and target, is a very good approximation [DF83].

The electron-nucleon interaction can be divided into a vertex which includes only electrons and a photon and a second vertex which couples the photon to the nuclear current. The first vertex is well understood by Quantum Electrodynamics (QED). However, the second vertex involving the nuclear current is much more difficult to calculate due to the dynamical structure of the nucleons and their interactions.

For these reasons, one often makes the assumption that the nuclear current is given by the sum of the currents of the individual nucleons, treated as free particles, the so called impulse approximation. This assumption is reasonable when the wavelength is smaller than the typical nucleon-nucleon distances within the nucleus. Moreover calculations of inclusive quasi elastic electron scattering, using the impulse approximation, usually predict the magnitude of the experimental cross section [DF83].

On the other hand one knows that this approximation must break down when going to larger wavelength. Experiments on oxygen have shown a decrease in the quasi elastic peak at beam energies of 700 MeV [A$^+$96]. Calculations from Benhar et al. can describe the reduction of the quasi elastic peak using a "state of the art" nucleon spectral function [BFN$^+$05]. This leads to the conclusion that "free" particles are not a good approximation in this energy region and nucleon-nucleon correlations become important. Furthermore, neutrino experiments at MiniBooNE [Min] have seen a deficit in the cross section at forward angles that recent models cannot describe.

The GiBUU transport model from Giessen [GiB] uses a Fermi gas model with

a momentum dependent mean field and Pauli blocking in the elementary nucleon reaction. The model can describe the electron data [A+96] for beam energies higher than 700 MeV. Furthermore, above the quasi elastic dominated region the model works even for the beam energy 700 MeV [BARLM07].

In this work, we will extend the GiBUU model by implementing short-range nucleon-nucleon correlations. We will examine the influence on quasi elastic processes of electron-nucleus scattering and neutrino-nucleus scattering. Furthermore, we will improve the initial state by replacing the Fermi gas by a more realistic momentum distribution that includes off shell particles in the nuclei.

This work is divided into three main parts. In chapter 2 we derive the in-medium spectral function for protons and neutrons that includes short-range nucleon-nucleon correlations using a self-consistent calculation.

The second part is devoted to the implementation of the in-medium modifications into the GiBUU code. Chapter 3 gives an overview of the mean field interaction used in the GiBUU model and chapter 4 deals with the numerical implementation of the spectral function with a finite width in the GiBUU code.

The final part of this work shows the modifications of the elementary cross section for electron and neutrino induced processes in chapter 5. Furthermore, we compare our calculation with the electron data from [A+96] and neutrino induced calculations from Benhar et al. [BFN+05]. Chapter 6 gives a summary of this work. A German summary can be found in appendix D.2.

2 Spectral Function in Nuclear Matter

As we know the nucleus consists out of many interacting nucleons. An accurate description of such a system requires the N-body wave function in configuration space containing all possible information, but a direct solution of the Schrödinger equation is not possible. Therefore, we use the Green's function method. Furthermore, this method simplifies the description of many identical particles [FW71].

The Green's function method allows us to concentrate on few matrix elements of interest. Moreover, the Green's function contains the most important physical quantities such as the energy and the lifetime of excited states. However, the exact Green's function is not easier to determine than the original wave function. Therefore we evaluate the Green's function in perturbation theory. It is possible to formulate an integral equation (Dyson equation) that yield the in-medium Green's function containing the interaction with the medium in the so called self-energy. The iteration of this process yield the self-consistently calculated width that will be used in the calculation of the electron and neutrino induced inclusive quasi-elastic cross sections of chapter 5.

2.1 Green's Functions

The in-medium spectral function can be calculated using the Green's function method. In this section we will get the major tools to deal with a many body system. Green's functions are described in many books on quantum field theory ([AGD63], [PS], [Bro],[Dic05],[KB62]) and are one of the basic concepts in modern many-body physics. A good overview of the self-consistent Green's function method can be found in [DB04].

2.1.1 Introduction to Green's functions

In quantum field theory the one-particle Green's function is one of the most important quantities characterizing the microscopic properties of a system [AGD63]:

$$g_{\alpha\beta}(x,x') = -i\langle 0|T(\psi_\alpha(x)\psi^\dagger_\beta(x')|0\rangle) \ , \tag{2.1}$$

with the four vector $x = (t,\vec{x})$, the spin indices α, β and the time-ordering operator T,

$$T(\psi(x)\psi^\dagger(y)) \equiv \begin{cases} \psi(x)\psi^\dagger(y) & \text{for } x^0 > y^0 \\ -\psi^\dagger(y)\psi(x) & \text{for } y^0 > x^0 \end{cases} .$$

The particle number density and the particle current density can be expressed in terms of Green's functions [AGD63]

$$n(x) = i \lim_{\substack{\vec{x}' \to \vec{x} \\ t' \to t+0}} g_{\alpha\alpha}(x, x') \tag{2.2}$$

$$j(x) = i \lim_{\substack{\vec{x}' \to \vec{x} \\ t' \to t+0}} (\nabla_{\vec{r}} - \nabla_{\vec{r}\,'}) g_{\alpha\alpha}(x, x') . \tag{2.3}$$

In general one can calculate the expectation value of one-particle operators using the Green's function method [AGD63]

$$\bar{F} = i \int d^3r \lim_{\substack{\vec{x}' \to \vec{x} \\ t' \to t+0}} f_{\alpha\beta}(x) g_{\alpha\beta}(x, x') . \tag{2.4}$$

In the following we will show that the poles of the Fourier transform of the Green's function determines the spectrum of the excitations. Moreover, we will see that the Green's function can be calculated using the diagram technique which has some advantages over the ordinary form of perturbation theory.

In this chapter we examine the general properties of the Green's function. Since we are interested in many-body physics we look at the example of a free Fermi gas. For simplicity the spin indices are dropped.

In the absence of an external field the Green's function depends only on the spacetime difference of the arguments and we can represent the Green's function as a Fourier integral [AGD63]

$$g(x - x') = \int \frac{d^4p}{(2\pi)^4} \; g(\omega, \vec{p}) e^{i[\vec{p}\cdot(\vec{r}-\vec{r}\,') - \omega(t-t')]} . \tag{2.5}$$

In the case of a non-interacting Fermi gas all states are filled up to the Fermi momentum p_f. Using the definition

$$\psi(\vec{r}, t) = \frac{1}{\sqrt{V}} \sum_{\vec{p}} a_{\vec{p}} \, e^{i[\vec{p}\cdot\vec{r} - \epsilon_0(\vec{p})t]} \tag{2.6}$$

in equation (2.1), we obtain for the Green's function

$$g^0(x) = -\frac{i}{V} \sum_{\vec{p}} e^{i[\vec{p}\cdot\vec{r} - \epsilon_0(\vec{p})t]} \begin{cases} 1 - n_{\vec{p}} & \text{for } t > 0 \\ -n_{\vec{p}} & \text{for } t < 0 \end{cases} \tag{2.7}$$

where the number density is defined as

$$n_{\vec{p}} =< a^{\dagger}_{\vec{p}}\, a_{\vec{p}} >= \begin{cases} 1 & \text{for } |\vec{p}| < p_f \\ 0 & \text{for } |\vec{p}| > p_f \end{cases} . \tag{2.8}$$

The Fourier transform of (2.7) is given by the relation

$$g^0(\omega,\vec{p}) = -i\left\{\theta(|\vec{p}|-p_f)\int_0^\infty dt\; e^{i[\omega t-\epsilon_0(\vec{p})t]} \; - \theta(p_f-|\vec{p}|)\int_0^\infty dt\; e^{-i[\omega t-\epsilon_0(\vec{p})t]}\right\} \tag{2.9}$$

This expression contains two integrals of the form

$$\int_0^\infty e^{ist}dt \; . \tag{2.10}$$

Since the integral is a Lebesgue integral the limit can be interchanged with the integration

$$\int_0^\infty e^{ist}dt = \int_0^\infty \lim_{\delta\to+0} e^{ist-\delta t}dt = \lim_{\delta\to+0}\int_0^\infty e^{ist-\delta t}dt \; . \tag{2.11}$$

Thus the integrand vanishes for $t \to \infty$ and we can evaluate the integral very easily:

$$\lim_{\delta\to+0}\int_0^\infty e^{ist-\delta t}dt = i\lim_{\delta\to+0}\frac{1}{s+i\delta} \; , \tag{2.12}$$

here $i\delta$ determines the way we bypass the pole at $s = 0$. Using the relation [KB62]

$$\int ds\; F(s)\frac{1}{s+i\delta} = \mathcal{P}\int ds\; \frac{F(s)}{s} \; - i\pi\; F(0) \tag{2.13}$$

we can write

$$\frac{1}{s+i\delta} = \frac{P}{s} - i\pi\delta(s) \; . \tag{2.14}$$

Using equation (2.12) the Green's function (2.9) can be brought into the form [AGD63]

$$g^0(\omega,\vec{p}) \;\; = \;\; \frac{\theta(|\vec{p}|-p_f)}{\omega-\epsilon_0(\vec{p})+i\delta} + \frac{\theta(p_f-|\vec{p}|)}{\omega-\epsilon_0(\vec{p})-i\delta} \; .$$

The only difference between the terms for $|\vec{p}| < p_f$ and $|\vec{p}| > p_f$ is the sign of δ. Thus, we can write the Green's function as

$$g^0(\omega,\vec{p}) \;\; = \;\; \frac{1}{\omega-\epsilon_0(\vec{p})+i\delta\;\mathrm{sgn}\;(|\vec{p}|-p_f)} \; . \tag{2.15}$$

2.1.2 Analytic Properties

We want to examine the analytic properties of the Green's function. Moreover we allow even Green's function for an interacting system. Consider a Fermionic system in the Schrödinger representation. For $t > t'$ the Green's function is given by [AGD63]

$$g(\vec{r}-\vec{r}\,',t-t')_{|_{t>t'}} = -i\langle 0|e^{i\hat{H}t}\psi(\vec{r})e^{-i\hat{H}(t-t')}\psi^\dagger(\vec{r}\,')e^{-i\hat{H}t'}|0\rangle \ . \quad (2.16)$$

Inserting unity $\mathbb{1} = \sum_n |n\rangle\langle n|$ in equation (2.16) yields

$$\begin{aligned} g(\vec{r}-\vec{r}\,',t-t')_{|_{t>t'}} &= -i\sum_n \langle 0|e^{i\hat{H}t}\psi(\vec{r})e^{-iHt}|n\rangle\langle n|e^{iHt'}\psi^\dagger(\vec{r}\,')e^{-i\hat{H}t'}|0\rangle \\ &= -i\sum_n e^{iE_0t}\underbrace{\langle 0|\psi(\vec{r})|n\rangle}_{\psi_{0n}}e^{-iE_nt}\ e^{iE_nt'}\underbrace{\langle n|\psi^\dagger(\vec{r}\,')|0\rangle}_{\psi^\dagger_{n0}}e^{-iE_0t'} \\ &= -i\sum_n \psi_{0n}(\vec{r})\psi^\dagger_{n0}(\vec{r}\,')e^{-i(E_n-E_0)(t-t')} \ . \end{aligned}$$

Analogue the Green's function can be calculated for $t < t'$. Thus, we obtain

$$g(\vec{r}-\vec{r}\,',t-t') = \begin{cases} -i\sum_n \psi_{0n}(\vec{r})\psi^\dagger_{n0}(\vec{r}\,')e^{-i(E_n-E_0)(t-t')} & \text{for } t > t' \\ i\sum_{n'} \psi^\dagger_{0n'}(\vec{r}\,')\psi_{n'0}(\vec{r})e^{i(E_{n'}-E_0)(t-t')} & \text{for } t < t' \end{cases} \quad (2.17)$$

For a homogeneous system the coordinate dependence is given by plane waves

$$\begin{aligned} \psi_{nm}(\vec{r}) &= \psi(0)e^{-i\vec{p}_{nm}\cdot\vec{r}} \\ \psi^\dagger_{nm}(\vec{r}) &= \psi^\dagger(0)e^{-i\vec{p}_{nm}\cdot\vec{r}} \ , \end{aligned}$$

where $\vec{p}_{nm} \equiv \vec{p}_n - \vec{p}_m$ and $\vec{p}_n$ is the momentum of the state n[1].

For $\vec{p}_m = 0$ one obtains [AGD63]

$$g(\vec{r}-\vec{r}\,',t-t') = \begin{cases} -i\sum_n |\psi(0)|^2 e^{i\vec{p}_n\cdot(\vec{r}-\vec{r}\,')}e^{-i(E_n-E_0)(t-t')} & \text{for } t > t' \\ \\ i\sum_{n'} |\psi(0)|^2 e^{-i\vec{p}_{n'}\cdot(\vec{r}-\vec{r}\,')}e^{i(E_{n'}-E_0)(t-t')} & \text{for } t < t' \end{cases} . \quad (2.18)$$

The operator $\psi^\dagger(0)$ increases the number of particles and $\psi(0)$ lowers the number of particles. Hence for $t > t'$ the summation with respect to n will be over states with particle number $N+1$, if the ground state has the particle number N

[1] One has to be careful with the indices $(\psi_{nm}(\vec{r}))^\dagger = \psi^\dagger_{mn}(\vec{r})$.

(see equation 2.17). For $t < t'$ the summation over n' is over states with particle number $N-1$. We choose a convenient notation [AGD63]

$$E_n(N+1) - E_0(N) = \epsilon_n + \mu \ , \tag{2.19}$$

with

$$\epsilon_n \equiv E_n(N+1) - E_0(N+1) \tag{2.20}$$
$$\mu \equiv E_0(N+1) - E_0(N) \ , \tag{2.21}$$

where ϵ_n is the excitation energy (which is positive by definition) and μ is the chemical potential at zero temperature $T = 0$. For $N-1$ we can write

$$\begin{aligned} E_{n'}(N-1) - E_0(N) &= E_{n'}(N-1) - E_0(N-1) - [E_0(N) - E_0(N-1)] \\ &= \epsilon_{n'} - \mu' \ . \end{aligned}$$

For large N we assume that $\epsilon_n = \epsilon_{n'}$ and $\mu = \mu'$, which leads to an error of order $\frac{1}{N}$.

The Fourier transform of (2.18) is given by

$$\begin{aligned} g(\vec{p},\omega) &= -i \int d^3x \int_0^\infty dt \sum_n |\psi(0)|^2 e^{i(\vec{p}_n - \vec{p})\cdot\vec{x}} e^{i(\omega - \epsilon_n - \mu)t} \\ &\quad + i \int d^3x \int_0^\infty dt \sum_{n'} |\psi(0)|^2 e^{-i(\vec{p}_{n'} + \vec{p})\cdot\vec{x}} e^{-i(\omega + \epsilon_{n'} - \mu)t} \ . \end{aligned} \tag{2.22}$$

Using equation (2.12) yields

$$\begin{aligned} g(\vec{p},\omega) &= \int d^3x \sum_n |\psi(0)|^2 e^{i(\vec{p}_n - \vec{p})\cdot\vec{x}} \frac{1}{\omega - \epsilon_n - \mu + i\delta} \\ &\quad + \int d^3x \sum_{n'} |\psi(0)|^2 e^{-i(\vec{p}_{n'} + \vec{p})\cdot\vec{x}} \frac{1}{\omega + \epsilon_n - \mu - i\delta} \ . \end{aligned} \tag{2.23}$$

The integration over d^3x gives

$$\begin{aligned} g(\vec{p},\omega) &= (2\pi)^3 \sum_n |\psi(0)|^2 \delta(\vec{p} - \vec{p}_n) \frac{1}{\omega - \epsilon_n - \mu + i\delta} \\ &\quad + (2\pi)^3 \sum_{n'} |\psi(0)|^2 \delta(\vec{p} + \vec{p}_n) \frac{1}{\omega + \epsilon_n - \mu - i\delta} \ . \end{aligned} \tag{2.24}$$

We can eliminate the sumation over n and n' by introducing the functions [AGD63]

$$A(\vec{p},E)dE = (2\pi)^3 \sum_n |\psi(0)|^2 \delta(\vec{p} - \vec{p}_n) \quad \text{for} \quad E < \epsilon_n < E + dE \tag{2.25}$$

$$B(\vec{p},E)dE = (2\pi)^3 \sum_{n'} |\psi(0)|^2 \delta(\vec{p} + \vec{p}_{n'}) \quad \text{for} \quad E < \epsilon_{n'} < E + dE \ . \tag{2.26}$$

These functions were first obtained by Lehman [Leh57] in a paper on quantum field theory. With these two functions we can collect all momenta that are on the same energy shell. Next, we sum up all energy shells, i.e. we integrate over the energy. Thus, we obtain

$$g(\vec{p},\omega) \;=\; \int_0^\infty \left[\frac{A(\vec{p},E)}{\omega - E - \mu + i\delta} + \frac{B(\vec{p},E)}{\omega + E - \mu - i\delta}\right] dE \;. \tag{2.27}$$

Separating the real and the imaginary part of the Green's function using

$$\int_0^\infty \frac{A(\vec{p},E)}{\omega - E - \mu + i\delta}\, dE \;=\; \int_0^\infty \frac{A(\vec{p},E)(\omega - E - \mu - i\delta)}{(\omega - E - \mu)^2 + \delta^2}\, dE$$

and

$$\begin{aligned}
\text{Re} \int_0^\infty \frac{A(\vec{p},E)}{\omega - E - \mu + i\delta}\, dE \;&=\; \int_0^\infty \frac{A(\vec{p},E)(\omega - E - \mu)}{(\omega - E - \mu)^2 + \delta^2} = P\int_0^\infty \frac{A(\vec{p},E)}{\omega - E - \mu}\, dE \;, \\
\text{Im} \int_0^\infty \frac{A(\vec{p},E)}{\omega - E - \mu + i\delta}\, dE \;&=\; -\int_0^\infty \frac{A(\vec{p},E)\delta}{(\omega - E - \mu)^2 + \delta^2}\, dE = \int_{\omega-\mu}^\infty \frac{A(\vec{p},z)\delta}{z^2 + \delta^2}\, dz \\
&=\; -\pi A(\vec{p},\omega - \mu) \text{ for } \omega > \mu \;,
\end{aligned}$$

we obtain [AGD63]

$$\text{Re } g(\vec{p},\omega) = P\int_0^\infty \left[\frac{A(\vec{p},E)}{\omega - E - \mu} + \frac{B(\vec{p},E)}{\omega + E - \mu}\right] dE$$

$$\text{Im } g(\vec{p},\omega) = \begin{cases} -\pi A(\vec{p},\omega - \mu) & \text{for } \omega > \mu \\ -\pi B(\vec{p},\mu - \omega) & \text{for } \omega < \mu \end{cases}.$$

Comparing the real and the imaginary part yields the relation [AGD63]

$$\text{Re } g(\vec{p},\omega) = \frac{P}{\pi}\int_{-\infty}^\infty \frac{\text{Im } G(\vec{p},\omega')\ \text{sgn }(\omega' - \omega)}{\omega' - \omega} d\omega \;. \tag{2.28}$$

For the following calculation it is useful to take a closer look at the analytic behavior of the Green's function. In equation (2.28) we can see that the Green's function is not analytic because of the factor sgn $(\omega' - \omega)$) which has no continuous derivative. However, it can be composed out of two analytic functions, the so called retarded Green's function g^R and the advanced Green's function g^A that are defined as [AGD63]

$$\text{Re } g \;=\; \text{Re } g^R = \text{Re } g^A$$

and

$$\begin{aligned} \text{Im } g^R &= \text{Im } g \text{ sgn } (\omega - \mu) && (2.29) \\ \text{Im } g^A &= -\text{Im } g \text{ sgn } (\omega - \mu) \, . && (2.30) \end{aligned}$$

Comparing equations (2.30) and (2.28) we can write for the retarded and advanced Green's functions

$$g^R(\vec{p}, \omega) = \begin{cases} g(\vec{p}, \omega) & \text{for } \omega > \mu \\ g^*(\vec{p}, \omega) & \text{for } \omega < \mu \end{cases}$$

$$g^A(\vec{p}, \omega) = \begin{cases} g^*(\vec{p}, \omega) & \text{for } \omega > \mu \\ g(\vec{p}, \omega) & \text{for } \omega < \mu \end{cases} .$$

In the Heisenberg representation the Green's functions g, g^R and g^A are defined as follows,

$$\begin{aligned} g(\vec{x}_1, t_1, \vec{x}_2, t_2) &\equiv \left\langle \, T[\Psi(\vec{x}_1, t_1)\Psi^\dagger(\vec{x}_2, t_2)] \, \right\rangle \\ g^R(\vec{x}_1, t_1, \vec{x}_2, t_2) &\equiv \begin{cases} -i \left\langle \left\{ \Psi(x_1, t_1), \Psi^\dagger(x_2, t_2) \right\} \right\rangle & \text{for } t_1 > t_2 \\ 0 & \text{for } t_1 < t_2 \end{cases} \\ g^A(\vec{x}_1, t_1, \vec{x}_2, t_2) &\equiv \begin{cases} 0 & \text{for } t_1 > t_2 \\ i \left\langle \left\{ \Psi^\dagger(x_1, t_1), \Psi(x_2, t_2) \right\} \right\rangle & \text{for } t_1 < t_2 \end{cases} , \end{aligned}$$

with

$$T[A(t_1)B(t_2)] \equiv \begin{cases} A(t_1)B(t_2) & \text{for } t_1 > t_2 \\ -B(t_2)A(t_1) & \text{for } t_2 > t_1 \end{cases} .$$

In our calculations we will use the one-particle Green's functions [KB62]

$$\begin{aligned} g^>(\vec{x}_1, t_1, \vec{x}_2, t_2) &\equiv -i \left\langle \Psi(\vec{x}_1, t_1)\Psi^\dagger(\vec{x}_2, t_2) \right\rangle && (2.31) \\ g^<(\vec{x}_1, t_1, \vec{x}_2, t_2) &\equiv i \left\langle \Psi^\dagger(\vec{x}_1, t_1)\Psi(\vec{x}_2, t_2) \right\rangle \, . && (2.32) \end{aligned}$$

These two Green's functions have the advantage that we do not have to take care of the time ordering or the sign of $t_1 - t_2$.

Using the definitions (2.31) and (2.32) one can show the following relations [Leh03]

$$\begin{aligned} (g^<(1,2))^* &= -g^<(1,2) \\ (g^>(1,2))^* &= -g^>(1,2) \\ \text{Im } g^R(1,2) &= -i\frac{1}{2}[g^R(1,2) - g^A(1,2)] \\ &= -\frac{1}{2}[g^>(1,2) - g^<(1,2)] \end{aligned}$$

where $(1,2) \equiv (\vec{x}_1, t_1, \vec{x}_2, t_2)$.

2.1.3 Physical Meaning of $g^<$ and $g^>$

One advantage of $g^<$ and $g^>$ is their physical interpretation. Considering $\vec{x}_1 = \vec{x}_2$ and $t_1 = t_2$, it follows from equation (2.31) and (2.32) that

$$g^<(\vec{x}, t) = i \left\langle \Psi^\dagger(\vec{x}, t)\Psi(\vec{x}, t) \right\rangle$$

is the number density of particles and

$$g^>(\vec{x}, t) = -i \left\langle \Psi(\vec{x}, t)\Psi^\dagger(\vec{x}, t) \right\rangle$$

is the number density of holes.

The arguments of Green's function coordinates can be split up into the relative coordinates $r_{\text{rel}} = (\, r^0_{\text{rel}}, \vec{r}_{\text{rel}}) = (t_1 - t_2, \vec{x}_1 - \vec{x}_2)$ and the center of mass coordinates $r_{\text{cm}} = (\, r^0_{\text{cm}}, \vec{r}_{\text{cm}}) = (\, (t_1 + t_2)/2, (\vec{x}_1 + \vec{x}_2)/2)$. The Fourier transform in the relative coordinates yields the Wigner transform [Leh03]

$$g^<(\omega, \vec{p}, r_{\text{cm}}) = \int d^4 r_{\text{rel}}\; e^{i(\omega r^0_{\text{rel}} - \vec{p}\cdot\vec{r}_{\text{rel}})} g^<(r_{\text{rel}}, r_{\text{cm}}) \;.$$

In a homogeneous and infinite system, the r_{cm} dependence vanishes and the Green's function depends only on $|\vec{p}|$. The total particle density can be calculated by integrating over $-ig^<$

$$\rho = -i \int \frac{d^4 p}{(2\pi)^4} g^<(p) \tag{2.33}$$

with $p = (\omega, \vec{p})$.

2.2 Spectral Function of a Free Fermi Gas

The spectral function is the central element of our approach. It is the function that will replace the on shell condition of the nucleon in the GiBUU calculation. With the spectral function we will determine the momentum distribution. This way, we take into account in-medium effects of protons and neutrons.

The spectral function is defined as [KB62]

$$\mathcal{A}(\omega, \vec{p}) = i[g^>(\omega, \vec{p}) - g^<(\omega, \vec{p})] = -2\text{Im}\; g^R(\omega, \vec{p}) \;, \tag{2.34}$$

and includes the spectral information of the whole system. For a fixed momentum the spectral function is normalized to

$$\int_{-\infty}^{\infty} \frac{d\omega}{2\pi}\; \mathcal{A}(\omega, p) = 1 \;. \tag{2.35}$$

The Green's functions $g^{\gtrless}$ can be expressed in terms of the spectral function

$$-ig^{<}(\omega,p) = \mathcal{A}(\omega,p)n(\omega,p) \ , \tag{2.36}$$
$$ig^{>}(\omega,p) = \mathcal{A}(\omega,p)(1-n(\omega,p)) \tag{2.37}$$

where $n(\omega,p)$ is the Fermi distribution function, i.e. the probability that the state with momentum p and energy ω is occupied. In the case of a non interacting Fermi gas at zero temperature $T=0$, all states up to the Fermi energy ω_F are filled and the Fermi distribution is a step function. Inserting the step function in (2.36) and (2.37) yields

$$-ig^{<}(\omega,p) = \mathcal{A}(\omega,p)\theta(\omega_f-\omega) \ , \tag{2.38}$$
$$ig^{>}(\omega,p) = \mathcal{A}(\omega,p)\theta(\omega-\omega_f) \ . \tag{2.39}$$

For free particles the spectral function is a δ -function. Using equation (2.38) with (2.33) leads to the relation

$$\begin{aligned}\rho &= \int \frac{d^3p d\omega}{(2\pi)^4}\theta(\omega_f-\omega)2\pi\delta(\omega-\frac{p^2}{2m}) \\ &= \frac{4\pi}{(2\pi)^3}\int_0^\infty dp\ p^2 = \frac{p_f^3}{6\pi^2}\end{aligned} \tag{2.40}$$

with the Fermi momentum $p_f = \sqrt{2m\omega_f}$. This leads to the famous Thomas-Fermi relation

$$p_f = (6\pi^2\rho)^{\frac{1}{3}} \ . \tag{2.41}$$

2.3 Self Energy

The Green's function describes the propagation of the particle. In the free case there are no collisions between two particles. This is different in an interacting medium. During the propagation of the particle it can interact with a different particle. This can lead to a shift in the energy because both particle attract each other or to a finite lifetime of the particle because of collisions. We will see that these effects will be taken into account by the so called self-energy that we will derive in this section.

We take into account only nucleon-nucleon interactions. The non relativistic Hamiltonian is given by [Dan84]

$$\hat{H} = \int d^3x\ \psi^\dagger(\vec{x})\left(-\frac{\nabla^2}{2m}\right)\psi(\vec{x}) + \frac{1}{2}\int d^3x \int d^3y\ \psi^\dagger(\vec{x})\psi^\dagger(\vec{y})v(\vec{x}-\vec{y})\psi(\vec{y})\psi(\vec{x}) \ , \tag{2.42}$$

with the nucleon-nucleon potential

$$v(\vec{x}_1-\vec{y}_2) \ . \tag{2.43}$$

Note, the interaction between the particles is not quantized in the Hamiltonian. The Green's function can be ordered in powers of interactions [Dic05] as shown in figure 2.1.

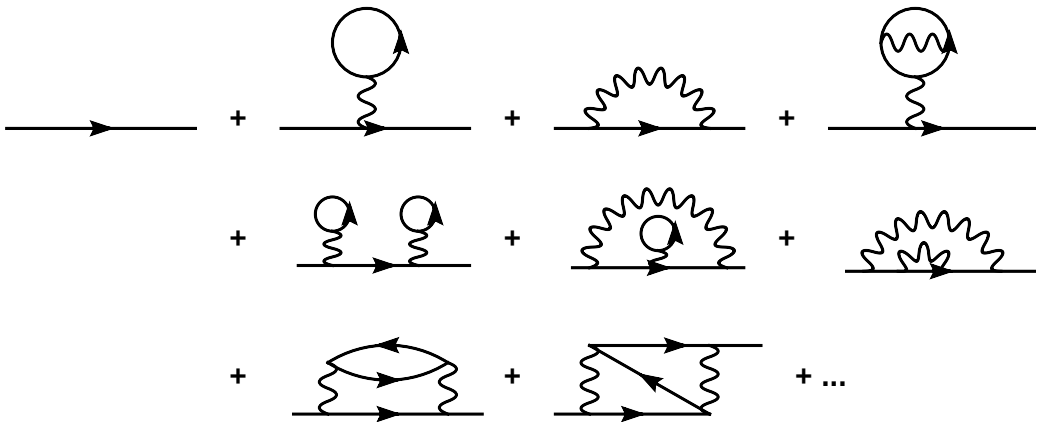

Figure 2.1: Self interaction with a two-point scalar potential in the Feynman diagram picture

We can reduce the number of diagrams by redefining the Green's function

$$g(1,1') = g^0(1,1') + \int d^4r_2 \; d^4r_3 \; g^0(1,2)\Sigma(2,3)g(3,1') \; , \tag{2.44}$$

where $g^0(1,1')$ is the Green's function of the free particle. Equation (2.44) is called Dyson equation. The self energy Σ contains the sum of all irreducible diagrams, i.e. all diagrams that cannot be separated into two or more diagrams of lower order. Dyson equation and self energy are illustrated in figure 2.2 and 2.3. We will solve the Dyson equation in section 2.4.

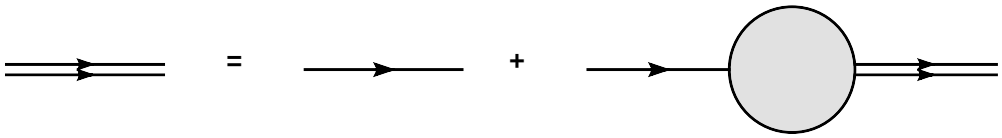

Figure 2.2: Diagrammatical representation of the Dyson equation

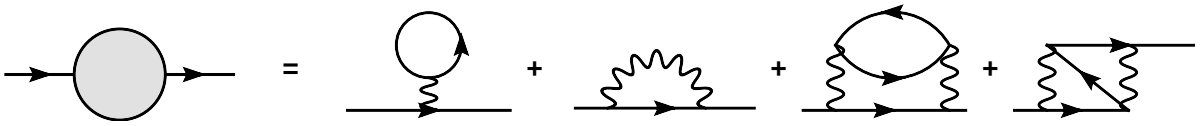

Figure 2.3: Diagrammatical representation of the self energy up to second order in perturbation theory

2.3.1 Hartree-Fock Self-Energy

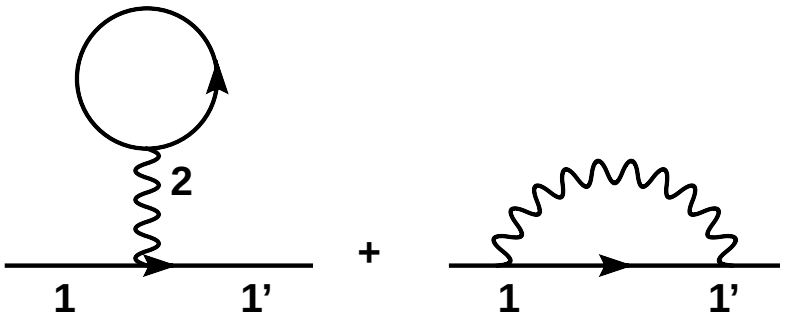

Figure 2.4: Hartree-Fock diagrams for the nucleon-nucleon interaction. Since the potential is local in time and the potential interacts directly with the incoming and outgoing particles one obtains an overall δ-function in time.

Figure 2.4 shows the lowest order contribution of the self energy. Using Feynman rules we obtain the analytic expression [Dan84]

$$\begin{aligned}\Sigma_{HF}(1,1') &= [\delta(\vec{r}_1-\vec{r}_{1'})\int d^3r_2\; v(\vec{r}_1-\vec{r}_2)(-i)g^0(\vec{r}_2,t_1,\vec{r}_2,t_1) \\ &\quad +v(\vec{r}_1-\vec{r}_{1'})ig^0(\vec{r}_1,t_1,\vec{r}_{1'},t_{1'})]\delta(t_1-t_{1'}) \qquad (2.45)\end{aligned}$$

These diagrams are called Hartree-Fock or mean-field self-energy. Since the potential is local in time and the potential interacts directly with the incoming and outgoing particles we obtain an overall δ-function in time. We are interested in the Wigner transform of equation 2.45). Due to the δ-function in time the integral can be evaluated very easily

$$\Sigma_{HF}(\omega) \propto e^{i\omega\cdot 0}\ .$$

Hence, the Wigner transform has no energy dependence. Since the self-energy is an analytic function we can use the following relations:

$$\text{Re}\ f(\omega) = \frac{1}{\pi}P\int_{-\infty}^{\infty} d\omega'\ \frac{\text{Im}\ f(\omega')}{\omega'-\omega} + C_\infty \qquad (2.46)$$

$$\text{Im}\ f(\omega) = -\frac{1}{\pi}P\int_{-\infty}^{\infty} d\omega'\ \frac{\text{Re}\ f(\omega')}{\omega'-\omega} + C'_\infty\ , \qquad (2.47)$$

where $f(\omega)$ is an analytic function. We already used these relations in equation (2.13). Since the Wigner transform is energy independent the imaginary part does not gain a dispersive part:

$$\begin{aligned}\text{Im}\ \Sigma_{HF} &= -\frac{1}{\pi}\text{Re}\ \Sigma_{HF}\underbrace{P\int_{-\infty}^{\infty} d\omega'\ \frac{1}{\omega'-\omega}}_{=0} + C'_\infty \\ &= C'_\infty\ .\end{aligned}$$

Hence, a constant in the real part does not generate an energy dependence in the imaginary part and vice versa.

The Green's function $g^0(1,1')$ of the free particle and the nucleon-nucleon potential $v(\vec{r}_1 - \vec{r}_2)$ depend only on $|\vec{r}_1 - \vec{r}_{1'}|$, due to Galilei invariance and rotational invariance. Furthermore, $(-i)g^0(\vec{r}_2, t_1, \vec{r}_2, t_1)$ is a real function, so that the Hartree-Fock part in coordinate space has the following properties:

$$\Sigma_{HF}(1,1') = \Sigma_{HF}(1',1) = (\Sigma_{HF}(1',1))^* \ .$$

The Wigner transform of the Hartree-Fock self-energy is given by

$$\begin{aligned}
\Sigma_{HF}(\omega, p) &= \int d^4 r_{\mathrm{rel}} \ e^{i(\omega r^0_{\mathrm{rel}} - \vec{p}\cdot\vec{r}_{\mathrm{rel}})} \Sigma_{HF}(r^0_{\mathrm{rel}}, \vec{r}_{\mathrm{rel}}) && (2.48)\\
&= \int d^4 r_{\mathrm{rel}} \ e^{-i(\omega r^0_{\mathrm{rel}} - \vec{p}\cdot\vec{r}_{\mathrm{rel}})} \Sigma_{HF}(-r^0_{\mathrm{rel}}, -\vec{r}_{\mathrm{rel}}) && (2.49)\\
&= \int d^4 r_{\mathrm{rel}} \ e^{-i(\omega r^0_{\mathrm{rel}} - \vec{p}\cdot\vec{r}_{\mathrm{rel}})} \Sigma_{HF}(r^0_{\mathrm{rel}}, \vec{r}_{\mathrm{rel}})^* && (2.50)\\
&= \Sigma^*_{HF}(\omega, p) && (2.51)
\end{aligned}$$

Thus, the Hartree-Fock part is energy independent and a real function:

$$\Sigma_{HF}(\omega, |\vec{p}|) = \Sigma_{HF}(|\vec{p}|) = \Sigma^*_{HF}(|\vec{p}|) \ . \quad (2.52)$$

2.3.2 Collision Term

Let us proceed to the second order self-energy diagrams. The diagrams are called Born diagrams. In figure 2.5 we obtain

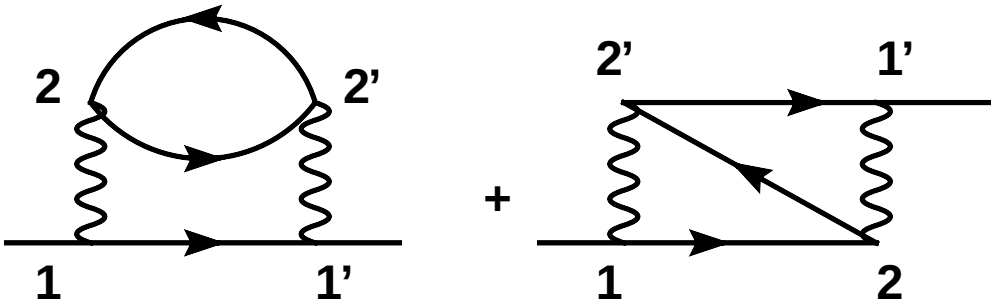

Figure 2.5: Born diagrams, left direct, right exchange term; Since there is no direct connection between the incoming and the outgoing particle through the potential, the Wigner transform of this diagram is energy dependent. Thus, we obtain a dispersive contribution to the imaginary part of the self-energy.

$$\Sigma_B(1,1') = \Sigma_{Bd}(1,1') + \Sigma_{Be}(1,1')$$

with

$$\Sigma_{Bd}(1,1') = \int d^3r_2\ d^3r_3\ v(\vec{r}_1-\vec{r}_2)v(\vec{r}_{2'}-\vec{r}_{1'})[g^0(1,1')g^0(2,2')g^0(2',2)]_{t_2=t_1;t_{2'}=t_{1'}}$$

$$\Sigma_{Be}(1,1') = -\int d^3r_2\ d^3r_3\ v(\vec{r}_1-\vec{r}_2)v(\vec{r}_{2'}-\vec{r}_{1'})[g^0(1,2)g^0(2,2')g^0(2',1')]_{t_2=t_1;t_{2'}=t_{1'}}\ .$$

In analogy to $g^>$ and $g^<$ we introduce the self-energies $\Sigma^{\gtrless}$,

$$\Sigma(1,2) = \theta(t_1-t_2)\Sigma^>(1,2) + \theta(t_2-t_1)\Sigma^<(1,2)\ . \tag{2.53}$$

After some algebra we get

$$\begin{aligned}\Sigma^{\gtrless}_{Bd}(1,1') &= \int d^3r_2\ d^3r_3\ v(\vec{r}_1-\vec{r}_2)v(\vec{r}_{2'}-\vec{r}_{1'}) \\ &\quad\times[g^{\gtrless}(1,1')g^{\gtrless}(2,2')g^{\lessgtr}(2',2)]_{t_2=t_1;t_{2'}=t_{1'}}\end{aligned} \tag{2.54}$$

and

$$\begin{aligned}\Sigma^{\gtrless}_{Be}(1,1') &= -\int d^3r_2\ d^3r_3\ v(\vec{r}_1-\vec{r}_2)v(\vec{r}_{2'}-\vec{r}_{1'}) \\ &\quad\times[g^{\gtrless}(1,2)g^{\lessgtr}(2,2')g^{\gtrless}(2',1')]_{t_2=t_1;t_{2'}=t_{1'}}\ .\end{aligned} \tag{2.55}$$

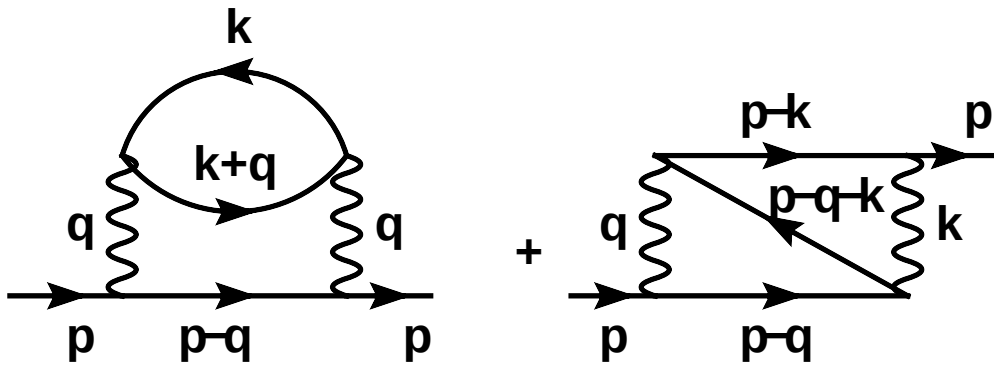

Figure 2.6: $\Sigma^>$ in momentum representation

In momentum representation we find in figure 2.6 for $\Sigma^>$ [KB62]

$$\begin{aligned}\Sigma^>(\omega,\vec{p}) &= \int \frac{d\omega_q d^3q}{(2\pi)^4}\frac{d\omega_k d^3k}{(2\pi)^4}v(q)^2 g^>(p-q)g^>(k+q)g^<(k) \\ &\quad -\int \frac{d\omega_q d^3q}{(2\pi)^4}\frac{d\omega_k d^3k}{(2\pi)^4}v(q)v(k)g^>(p-q)g^>(p-k)g^<(p-q-k)\end{aligned}$$

(2.56)

Substituting $k' = p - q - k$ in the second term yields

$$\begin{aligned} \Sigma^{>}(\omega, \vec{p}) &= \int \frac{d\omega_q d^3q}{(2\pi)^4} \frac{d\omega_k d^3k}{(2\pi)^4} \left[v(q)^2 - v(q)v(p-q-k) \right] \\ &\quad \times g^{>}(p-q) g^{>}(k+q) g^{<}(k) \end{aligned} \tag{2.57}$$

and we get

$$\Sigma^{>}(\omega, \vec{p}) = \int \frac{d\omega_q d^3q}{(2\pi)^4} \frac{d\omega_k d^3k}{(2\pi)^4} |\mathcal{M}|^2 \; g^{>}(p-q) g^{>}(k+q) g^{<}(q) \tag{2.58}$$

with

$$|\mathcal{M}|^2 = \frac{1}{2}[v(q) - v(p-q-k)]^2 \; . \tag{2.59}$$

We can calculate $\Sigma^{<}$ in the same way

$$\Sigma^{<}(\omega, \vec{p}) = \int \frac{d\omega_q d^3q}{(2\pi)^4} \frac{d\omega_k d^3k}{(2\pi)^4} |\mathcal{M}|^2 \; g^{<}(p-q) g^{<}(k+q) g^{>}(q) \; . \tag{2.60}$$

We can see in (2.58) and (2.60) that the Born diagrams are non-local in time and in space. Thus, we will get an energy dependence. As we seen in subsection 2.3.1 a constant in the real part cannot generate a energy dependence in the imaginary part and vice versa for an analytic function. Hence, we obtain a non-zero energy dependent real and imaginary part of the self energy that leads to a shift of the pole and a broadening of the spectral function,

$$\text{Im } \Sigma_B \neq 0 \; .$$

The real part and the imaginary part of the self-energy are related by the Kramers-Kroening relation [KB62]

$$\text{Re } \Sigma_B^R(\omega, \vec{p}) = -P \int \frac{d\omega'}{\pi} \frac{\text{Im } \Sigma_B^R(\omega', \vec{p})}{\omega - \omega'} \; ,$$

which is the dispersive part of equation (2.47). We define the width, that will be used later in the spectral function, as

$$\Gamma = -2\text{Im } \Sigma^R \; . \tag{2.61}$$

2.3.3 Meaning of $\Sigma^{\gtrless}$

We can express equations (2.58) and (2.60) in terms of [Leh03]

$$\begin{aligned}\Sigma^{>}(\omega,\vec{p}) &= \int \frac{d\omega_2 d^3p_2}{(2\pi)^4}\frac{d\omega_3 d^3p_3}{(2\pi)^4}\frac{d\omega_4 d^3p_4}{(2\pi)^4} \\ &\quad\times(2\pi)^4\delta(\vec{p}+\vec{p}_2-\vec{p}_3-\vec{p}_4)\delta(\omega+\omega_2-\omega_3-\omega_4) \\ &\quad\times|\mathcal{M}|^2\; g^{<}(\omega_2,\vec{p}_2)g^{>}(\omega_3,\vec{p}_3)g^{>}(\omega_4,\vec{p}_4) \qquad (2.62)\end{aligned}$$

and

$$\begin{aligned}\Sigma^{<}(\omega,\vec{p}) &= \int \frac{d\omega_2 d^3p_2}{(2\pi)^4}\frac{d\omega_3 d^3p_3}{(2\pi)^4}\frac{d\omega_4 d^3p_4}{(2\pi)^4} \\ &\quad\times(2\pi)^4\delta(\vec{p}+\vec{p}_2-\vec{p}_3-\vec{p}_4)\delta(\omega+\omega_2-\omega_3-\omega_4) \\ &\quad\times|\mathcal{M}|^2\; g^{>}(\omega_2,\vec{p}_2)g^{<}(\omega_3,\vec{p}_3)g^{<}(\omega_4,\vec{p}_4) \qquad (2.63)\end{aligned}$$

From section 2.1 we know that $-ig^{<}(\omega,p)$ is the number density of the occupied states and $-ig^{>}(\omega,p)$ is the number density of the unoccupied states. Therefore, $\Sigma^{>}(\omega,\vec{p})$ can be identified with the total collision rate out of the state $(\omega,\vec{p})$ (See figure 2.7). A particle with momentum p and energy ω and a particle with momentum p_2 and energy ω_2 collide and populate the two unoccupied states (ω_3,p_3) and (ω_4,p_4). Since we are interested in the total collision rate of the state $(\omega,\vec{p})$, we integrate over p_2, p_3 and p_4, and ω_2, ω_3, ω_4.

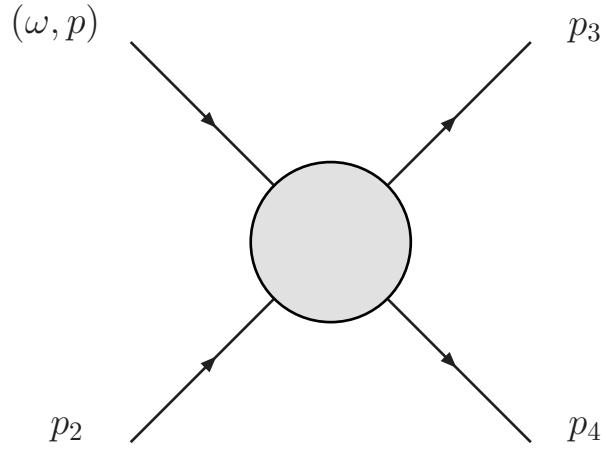

Figure 2.7: Physical interpretation of $\Sigma^{>}$: $\Sigma^{>}(\omega,\vec{p})$ can be identified with the total collision rate out of the state $(\omega,\vec{p})$

$\Sigma^{<}(\omega,\vec{p})$ can be identified with the total production rate of the state $(\omega,\vec{p})$ (See figure 2.8). The particles (ω,p) and (ω_2,p_2) are produced in the collision of

the two particles (ω_3, p_3) and (ω_4, p_4). In order to get the total production rate we integrate over p_2, p_3 and p_4, and ω_2, ω_3, ω_4.

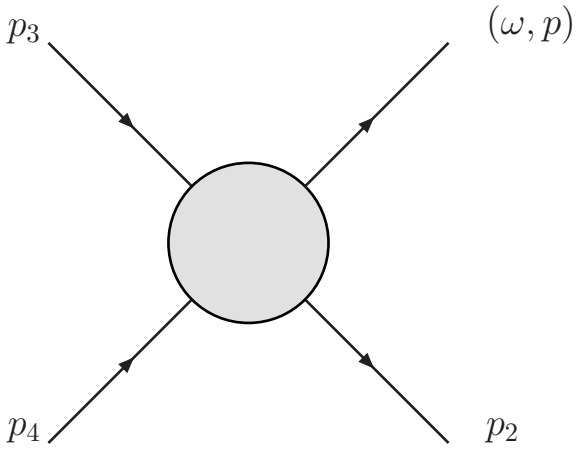

Figure 2.8: Physical interpretation of $\Sigma^<$: $\Sigma^<(\omega, \vec{p})$ can be identified with the total production rate of the state $(\omega, \vec{p})$

2.4 Green's Function and the Spectral Function in Infinite Matter

We want to solve the Dyson equation (2.44). First, we note that the Green's function $g(1, 1')$ depends only on the difference $(x_1 - x_{1'})$ between the two points with $x_1 = (t_1, \vec{x}_1)$ and $x_{1'} = (t_{1'}, \vec{x}_{1'})$. We multiply (2.44) with $(i\frac{\partial}{\partial t_1} + \frac{\nabla_1^2}{2m})$

$$\begin{aligned}(i\frac{\partial}{\partial t_1} + \frac{\nabla_1^2}{2m})g(x_1 - x_1') &= \delta^4(x_1 - x_{1'}) + \int d^4r\ \Sigma(x_1 - r)g(r - x_{1'}) \\ &= \delta^4(x_1 - x_{1'}) + \int d^4y\ \Sigma(x_1 - x_{1'} - y)g(y)\ .\end{aligned}$$

The Fourier transform is [2]

$$\begin{aligned}\int d^4z\ (i\frac{\partial}{\partial t_1} + \frac{\nabla_1^2}{2m})g(z)e^{-i(\omega z^0 - \vec{p}\cdot\vec{z})} &= 1 + \int d^4z d^4y\ \Sigma(z - y)g(y)e^{-i(\omega z^0 - \vec{p}\cdot\vec{z})} \\ (\omega - \frac{p^2}{2m})g(\omega, p) &= 1 + \Sigma(\omega, p)g(\omega, p)\end{aligned}$$

with $z = (t_1 - t_{1'}, \vec{x}_1 - \vec{x}_{1'})$.
From the Fourier transform, we obtain the in-medium Green's function

$$g(\omega, \vec{p}) = \frac{1}{\omega - \frac{\vec{p}^2}{2m} - \Sigma(\omega, \vec{p})}\ . \tag{2.64}$$

[2] We use the convolution theorem $\mathcal{F}[f * g] = \mathcal{F}f \cdot \mathcal{F}g$ with $[f * g](t) = \int d\tau\ f(t - \tau)g(\tau)$

Inserting the Green's function in the definition of the spectral function (2.34) yields

$$\begin{aligned}\mathcal{A}(\omega,\vec{p}) &= -i\left(\frac{1}{\omega-\frac{\vec{p}}{2m}-\text{Re }\Sigma^R(\omega,\vec{p})-i\text{Im }\Sigma^R(\omega,\vec{p})}\right)^* \\ &\quad +i\frac{1}{\omega-\frac{\vec{p}}{2m}-\text{Re }\Sigma^R(\omega,\vec{p})-i\text{Im }\Sigma^R(\omega,\vec{p})} \\ &= -i\frac{(\omega-\frac{\vec{p}}{2m}-\text{Re }\Sigma^R(\omega,\vec{p}))-i\text{Im }\Sigma^R(\omega,\vec{p})}{(\omega-\frac{\vec{p}^2}{2m}-\text{Re }\Sigma^R(\omega,\vec{p}))^2+\text{Im }\Sigma^R(\omega,\vec{p})^2} \\ &\quad +i\frac{(\omega-\frac{\vec{p}}{2m}-\text{Re }\Sigma^R(\omega,\vec{p}))+i\text{ Im }\Sigma^R(\omega,\vec{p})}{(\omega-\frac{\vec{p}^2}{2m}-\text{Re }\Sigma^R(\omega,\vec{p}))^2+\text{Im }\Sigma^R(\omega,\vec{p})^2}\end{aligned}$$

$$\mathcal{A}(\omega,\vec{p})=\frac{-2\text{Im }\Sigma^R(\omega,\vec{p})}{(\omega-\frac{\vec{p}^2}{2m}-\text{Re }\Sigma^R(\omega,\vec{p}))^2+\text{Im }\Sigma^R(\omega,\vec{p})^2} \tag{2.65}$$

In the Hartree-Fock approximation the self energy is real and shifts the pole of the spectral function. Since Im $\Sigma_{HF}(\omega,\vec{p})=0$, the spectral function is still a δ-function [Leh03],

$$\mathcal{A}_{HF}(\omega,\vec{p})=2\pi\ \delta\left(\omega-\frac{\vec{p}^2}{2m}-\text{Re }\Sigma_{HF}(|\vec{p}|)\right)\ . \tag{2.66}$$

In second order, the imaginary part of the self energy is not zero. Hence, we obtain a Breit-Wigner form for the spectral function [Leh03],

$$\mathcal{A}(\omega,\vec{p})=\frac{\Gamma(\omega,\vec{p})}{(\omega-\frac{\vec{p}^2}{2m}-\text{Re }\Sigma(\omega,\vec{p}))^2+\frac{\Gamma(\omega,\vec{p})^2}{4}} \tag{2.67}$$

with

$$\text{Re }\Sigma(\omega,\vec{p}) = \Sigma_{HF}(|\vec{p}|)+P\int\frac{d\omega}{2\pi}\frac{\Gamma(\omega,\vec{p})}{\omega-\omega'} \tag{2.68}$$

$$\Gamma(\omega,\vec{p}) = -2\text{ Im }\Sigma_B(\omega,\vec{p})\ . \tag{2.69}$$

2.5 Numerical Details

To find the second order self-energy we have to evaluate equations (2.62) and (2.63). Choosing a constant matrix element, i.e. a pointlike interaction in coordinate space, simplifies the self energy calculation. The equations (2.62) and

(2.63) turn into

$$\begin{aligned}\Sigma^{>}(\omega,\vec{p}) &= |\mathcal{M}|^2 \int \frac{d\omega_2 d^3p_2}{(2\pi)^4}\frac{d\omega_3 d^3p_3}{(2\pi)^4}\frac{d\omega_4 d^3p_4}{(2\pi)^4} \\ &\times(2\pi)^4\delta(\vec{p}+\vec{p}_2-\vec{p}_3-\vec{p}_4)\delta(\omega+\omega_2-\omega_3-\omega_4) \\ &\times\ g^{<}(\omega_2,\vec{p}_2)g^{>}(\omega_3,\vec{p}_3)g^{>}(\omega_4,\vec{p}_4) \end{aligned} \tag{2.70}$$

and

$$\begin{aligned}\Sigma^{<}(\omega,\vec{p}) &= |\mathcal{M}|^2 \int \frac{d\omega_2 d^3p_2}{(2\pi)^4}\frac{d\omega_3 d^3p_3}{(2\pi)^4}\frac{d\omega_4 d^3p_4}{(2\pi)^4} \\ &\times(2\pi)^4\delta(\vec{p}+\vec{p}_2-\vec{p}_3-\vec{p}_4)\delta(\omega+\omega_2-\omega_3-\omega_4) \\ &\times\ g^{>}(\omega_2,\vec{p}_2)g^{<}(\omega_3,\vec{p}_3)g^{<}(\omega_4,\vec{p}_4)\ . \end{aligned} \tag{2.71}$$

Evaluating the delta-function in the equations (2.70) and (2.71) yields

$$\begin{aligned}\Sigma^{<}(\omega,\vec{p}) &= +i\frac{|\mathcal{M}|^2}{(2\pi)^6}\int d\omega_2\ \int d\omega_3\ \int dp_3\ p_3^2\ \int dp_2\ p_2^2\frac{d\cos\theta_2}{p_{tot}p_3} \\ &\times\mathcal{A}(\omega_2,p_2)f(\omega_2,p_2)\mathcal{A}(\omega_3,p_3)(1-f(\omega_3,p_3)) \\ &\times\int dp_4 p_4\mathcal{A}(\omega_4,p_4)(1-f(\omega_4,p_4))\ , \end{aligned} \tag{2.72}$$

and

$$\begin{aligned}\Sigma^{>}(\omega,\vec{p}) &= -i\frac{|\mathcal{M}|^2}{(2\pi)^6}\int d\omega_2\ \int d\omega_3\ \int dp_3\ p_3^2\ \int dp_2\ p_2^2\frac{d\cos\theta_2}{p_{tot}p_3} \\ &\times\mathcal{A}(\omega_2,p_2)(1-f(\omega_2,p_2))\mathcal{A}(\omega_3,p_3)f(\omega_3,p_3) \\ &\times\int dp_4 p_4\mathcal{A}(\omega_4,p_4)f(\omega_4,p_4)\ , \end{aligned} \tag{2.73}$$

with $p_{tot} = |\vec{p}+\vec{p}_2|$ and $\omega_4 = \omega+\omega_2-\omega_3$.

Calculations from J. Lehr [Leh03], P. Konrad [KLM05],[Kon04] and F. Frömel [Fro01] have shown that for short-range effects one obtains results with constant matrix elements that are comparable with the results of the sophisticated many-body calculations of Benhar et al. [BFF89]. Since we use the same Skyrme parameters as in [KLM05] we use the averaged matrix element

$$|\mathcal{M}| = 350\ \text{MeVfm}^3\ . \tag{2.74}$$

This value is in the region that is derived by Landau-Migdal parameters ($|\mathcal{M}| = 341\ \text{MeVfm}^3$) [KLM05] and comparisons with Benhar et al. [BFF89] ($|\mathcal{M}| =$

320 MeVfm^3) [KLM05]. Further comparisons with Benhar have shown that one obtains even better results for the chosen matrix element of $|\mathcal{M}| = 350$ MeVfm^3 . Since we will use the spectral function in GiBUU for oxygen $^{16}_{8}$O we calculate the spectral function for isospin symmetric matter. For our calculations we choose a grid in the energy and momentum plane with the limits -0.5 GeV $\leq \omega \leq 0.5$ GeV and $p \leq 1.25$ GeV/c. The spacing is in both directions 5.0 MeV. The finite size of the grid leads to a cutoff in energy and momentum at the boundaries. This leads to a lack of information on the behavior of the spectral function at energies outside the grid limits. In order to calculate the real part of the self-energy by the dispersion relation (2.68), the imaginary part is extrapolated into the regions of large energies by assuming a Gaussian tail.

We calculate the spectral function self-consistently. Therefore we estimate a starting width and calculate the self-energy numerically from equations (2.72) and (2.73). With this result we calculate a new spectral function that is the input of the next iteration:

$$\Gamma(\omega,\vec{p}) \rightarrow \mathcal{A}(\omega,\vec{p}) \rightarrow \Sigma(\omega,\vec{p}) \rightarrow \Gamma(\omega,\vec{p}), \mathrm{Re}\ \Sigma \rightarrow \ldots$$

In our calculation we take into account the dispersive part of the self-energy. After some iterations (3 to 5 iterations) the spectral function does not change anymore. In the picture of Feynman diagrams, our self-consistent calculation corresponds to a resummation of the Born diagrams to all orders.

The integration over the quasi-particle peak of the spectral is not trivial. The on-shell peaks of the spectral function are narrow structures compared to the full integration volume. The integration routine is explained in appendix C.

The mean field effects are taken into account by the effective potential and the effective mass. The parameters are taken from the Skyrme SLy230a [CMB+97] interaction. By executing the variation of the energy density functional with respect to the kinetic energy density τ_q and the nucleon density ρ_q, where $q = n, p$, one obtains for the effective mass and for the effective potential [KLM05]:

$$\frac{m_q}{m_q^*} = 1 + \frac{2m_q}{\hbar^2}\left(\frac{1}{8}[t_1(2+x_1) + t_2(2+x_2)]\rho + \frac{1}{8}[t_2(2x_2+1) - t_1(2x_1+1)]\rho_q\right) , \tag{2.75}$$

$$\begin{aligned} U_q^{eff} = {} & \frac{1}{4}t_0[2(2+x_0)\rho - 2(2x_0+1)\rho_q] \\ & + \frac{1}{24}t_3\rho^\sigma[2(2+x_3)\rho - 2(2x_3+1)\rho_q] \\ & + \frac{1}{24}\sigma t_3\rho^{\sigma-1}[(2+x_3)\rho^2 - (2x_3+1)(\rho_q^2+\rho_n^2)] \\ & + \frac{1}{8}[t_1(2+x_1) + t_2(2+x_2)]\tau \\ & + \frac{1}{8}[t_2(2x_2+1) - t_1(2x_1+1)]\tau_q , \end{aligned} \tag{2.76}$$

t_0 (MeVfm^3)	-2490.23
t_1 (MeVfm^5)	489.53
t_2 (MeVfm^5)	-566.58
t_3 (MeVfm$^{2+3\sigma}$)	13803.0
x_0	1.1318
x_1	-0.8426
x_2	-1.0
x_3	-1.9219
σ	1/6

Table 2.1: Parameters of the Skyrme SLy230a [CMB+97] interaction.

where ρ is the total and τ the total kinetic density. The Skyrme parameters x_0, x_1, x_2, x_3, t_0, t_1, t_2, t_3 and σ are given in table 2.1. The Feri energy at the saturation density $\rho_0 = -0.16$ fm^{-3} is $\omega_F = -16$ MeV. For further details see [Kon04] and [KLM05].

2.6 Results for the Spectral Function

Figure 2.9 shows the spectral function and the corresponding width as functions of the energy at the saturation density $\rho_0 = 0.16\text{fm}^{-3}$. The momentum $p = 0.1667$ GeV/c is chosen to be below the Fermi momentum $p_F = 0.27$ GeV/c. The quasi particle peak is located below the Fermi energy at $E_{\vec{p}} = -0.041$ GeV. In the mean field approximation this peak would be a delta function. Due to the short-range correlations coming from the second order diagrams discussed in section 2.3.2, we observe a broadening of the quasi elastic peak. The spectral function as well as the width drops to zero at the Fermi energy. Furthermore the spectral function has some strength located above the Fermi energy because of the non-zero width above the Fermi energy. Due to the dispersion relation (2.68) the spectral function is normalized to one for on-shell peaks below the upper boundary of the energy. For higher energies the normalization is not possible anymore due to the finite size of the grid.

Since the states at the Fermi energy are stable, due to kinematical constraints, it is not possible to scatter into or out of those states and thus the width is zero. Below the Fermi energy the width is dominated by two-particle one-hole excitations, i.e. $\Sigma^<$ and above the Fermi energy the width is dominated by one-particle two-hole excitations, i.e. $\Sigma^>$ (More details can be found in appendix D). At low energies the width starts almost constant at $\Gamma = 0.016$ GeV. It reaches a local maximum of $\Gamma = 0.029$ GeV at -0.1 GeV; after that it drops into the valley around the Fermi energy. Above the Fermi energy the width rises rapidly. At the grid boundary it has the value $\Gamma = 0.162$ GeV. With higher energy the phase space of the excited particles in $\Sigma^>$ increases because one has more possibilities

to distribute the energy. Thus, the width increases.

In figure 2.10 we show the spectral function and the corresponding width as functions of the energy at the saturation density. The momentum $p = 0.3333$ GeV/c is chosen to be above the Fermi momentum. We see that the quasi elastic peak is located above the Fermi energy. Here we find strength below p_F that would not be there in a pure mean-field approximation. Since the width below the Fermi energy is smaller than the width above the Fermi energy, the tail of the spectral function below the Fermi energy is smaller than the tail in figure 2.9.

Since most of the strength of the spectral function is located around the on-shell peak the on-shell width has a strong influence on integrations over the spectral function. Figure 2.11 shows the on-shell width $\Gamma_{on}(E) = \Gamma(E, p(E))$ as a function of $E - E_F$, where E_F is the Fermi energy and $p(E) = (2m^*(E - U_{eff}))^{1/2}$. The solid black line shows the result of the on-shell width of our calculation, the dashed line shows the result of Benhar et al. [BFF89], [BFF92], the dotted line shows the result of Baldo et al. [BBG$^+$92] and the dash dotted line shows the result of Froemel [FLM03]. It can be seen that our result is in between the calculation of Benhar and Baldo, and Froemel.

Figure 2.12 shows the self-consistently calculated width as a function of the momentum at fixed energy $E = -33$ MeV that is below the Fermi energy. Since the energy is below the Fermi energy the width is dominated by $\Sigma^<$. Below $p = 0.18$ GeV/c the width is almost constant ($\Gamma \approx 0.006$ GeV). Between $p = 0.18$ GeV/c and $p = 0.8$ GeV/c the width drops to zero. This drop is due to the fact that for higher momenta the overlap between the particle excitations and the hole excitations become smaller such that $\Sigma^<$ decreases. For more information see appendix D. The plateau below $p = 0.18$ GeV/c comes from Pauli-blocking that limits the volume of the phase space.

Figure 2.13 shows the self-consistently calculated width as a function of the momentum at fixed energy $E = 83$ MeV that is above the Fermi energy. Since the energy is above the Fermi energy the width is dominated by $\Sigma^>$ and thus the width is bigger compared to figure 2.12. The drop is due to the fact that for higher momenta the overlap between the particle excitations and the hole excitations becomes smaller such that $\Sigma^<$ decreases. For more information see appendix D. The plateau below $p = 0.18$ GeV/c comes from Pauli-blocking that limits the volume of the phase space and separates the particle and hole excitations so that the overlap of the spectral functions cannot increase.

In order to use the nuclear matter results for a real nucleus we have to calculate the width for different densities. Figure 2.14 shows the self-consistently calculated width for different densities as a function of the energy for the fixed momentum $p = 0.01667$ GeV/c. We can see that the width scales approximately with a constant factor for low densities. For higher densities, we observe a saturation of the width above the Fermi energy. Furthermore, a constant scaling factor cannot be determined anymore.

For low densities we expect that the width rises linearly in density. That is

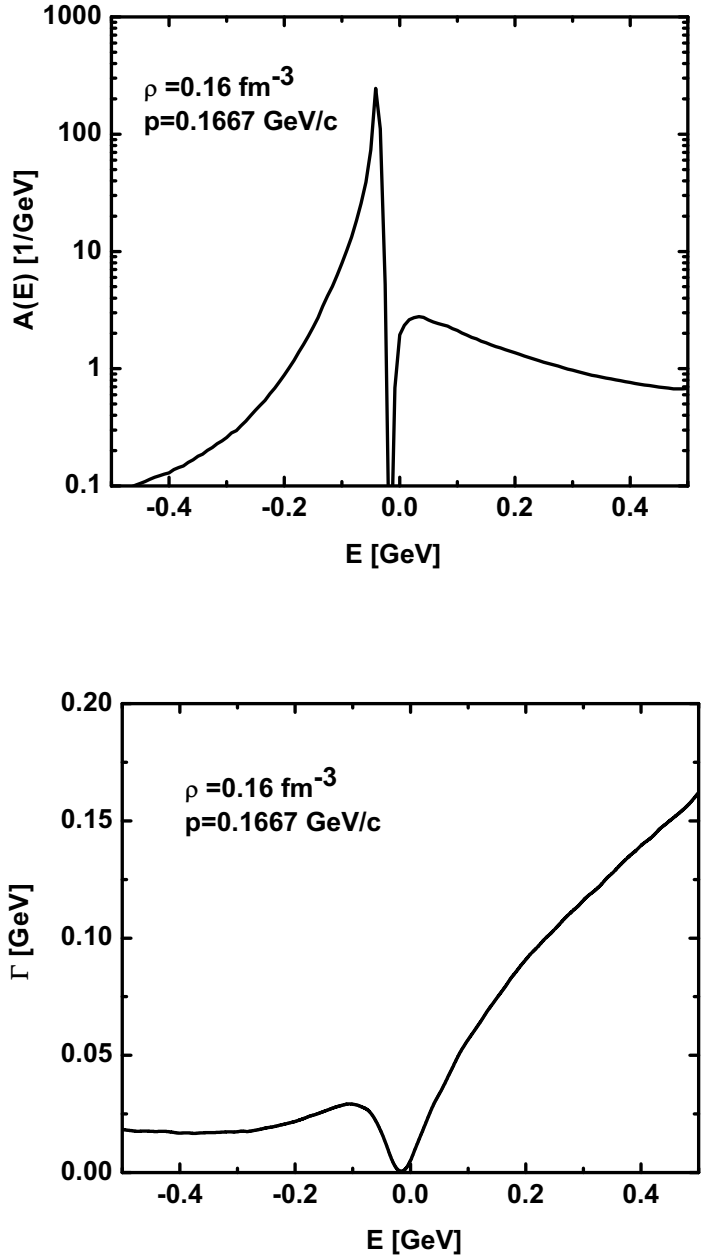

Figure 2.9: Cut through the spectral function, including the dispersive part of the self-energy, and the corresponding width for isospin symmetric matter at fixed momentum below $p_f = 0.27$ GeV/c.

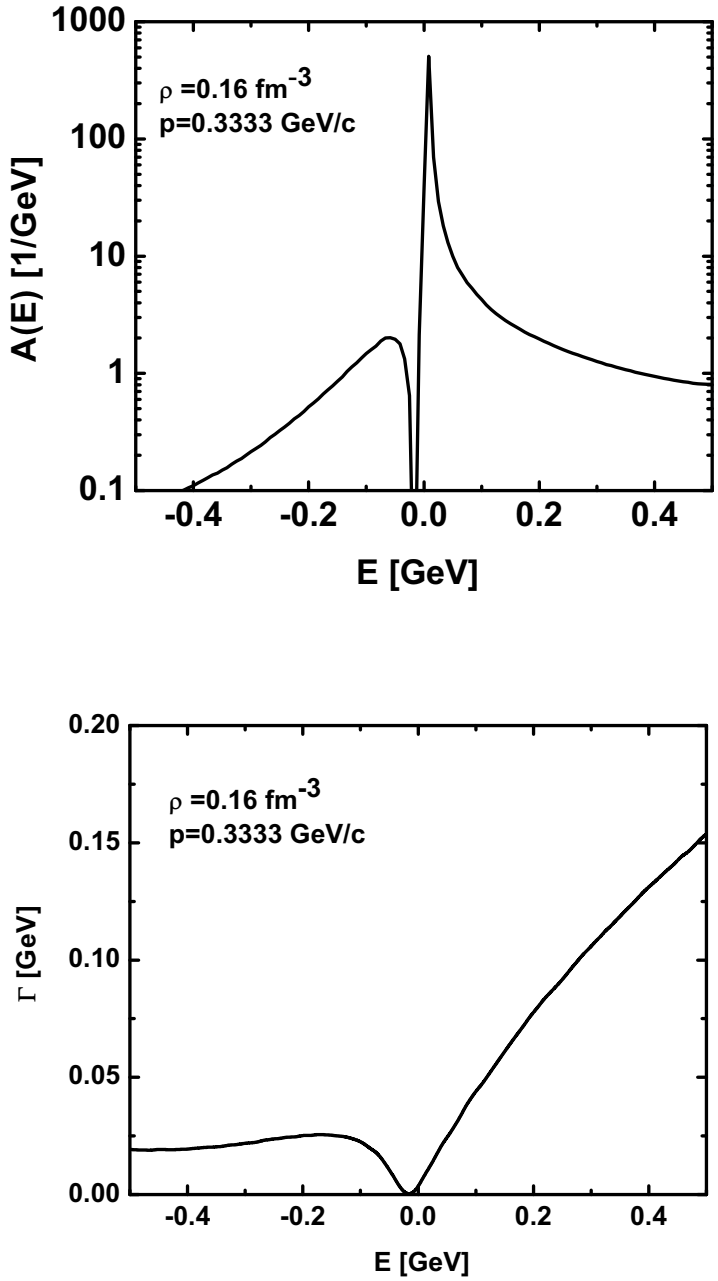

Figure 2.10: Cut through the spectral function, including the dispersive part of the self-energy, and the corresponding width for isospin symmetric matter at fixed momentum above $p_f = 0.27$ GeV/c.

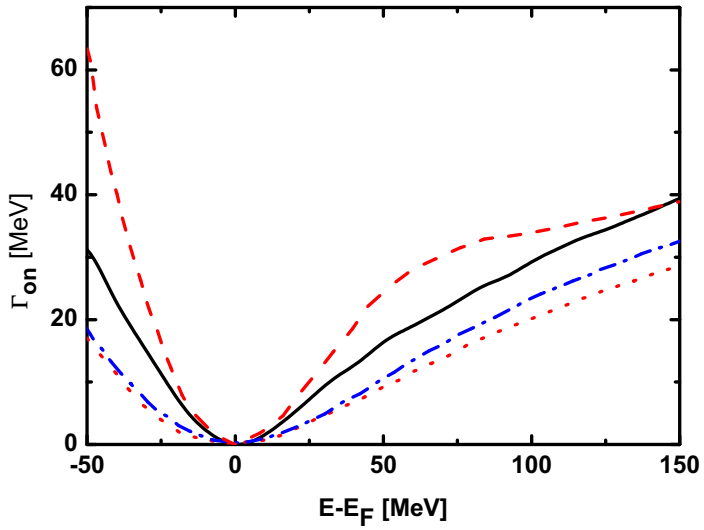

Figure 2.11: The on-shell width $\Gamma_{on}(E)$ as a function of $E - E_F$ with the Fermi energy E_F for the nuclear matter density $\rho = \rho_0$. The solid black line shows the result of our calculation, the dashed line the result of Benhar et al. [BFF89], [BFF92], the dotted line the result of Baldo et al. [BBG$^+$92] and the dash dotted line the result of Froemel [FLM03] .

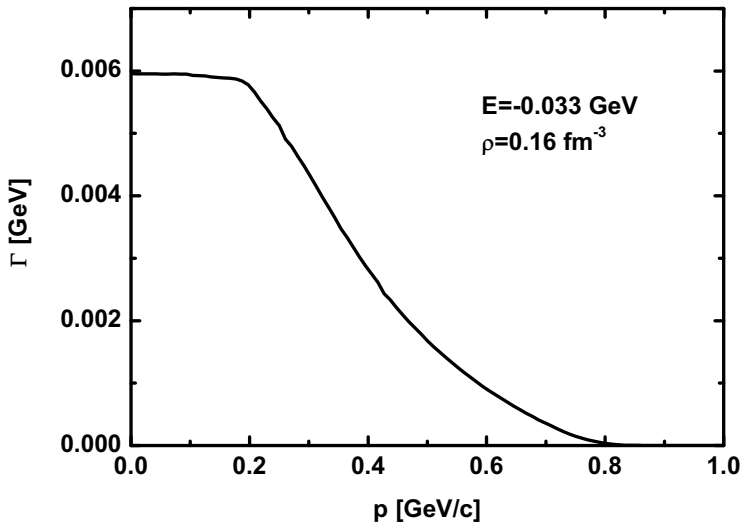

Figure 2.12: Self-consistently calculated width, including the dispersive part of the self-energy, as a function of the momentum at fixed energy $E = -0.033$ GeV and at the saturation density $\rho_0 = 0.16$ fm^{-3}.

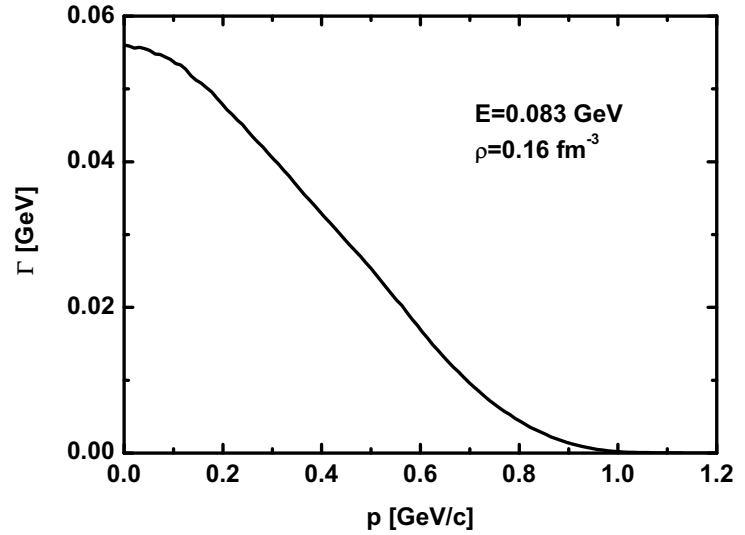

Figure 2.13: Self-consistently calculated width, including the dispersive part of the self-energy, as a function of the momentum at fixed energy $E = -0.033$ GeV and at the saturation density $\rho_0 = 0.16$ fm^{-3}.

due to the fact that for low densities the width is determined by the number of particles. For higher densities Pauli blocking becomes important such that particles far below the Fermi energy does not contribute to the collision width. Figure 2.15 shows the self-consistently calculated width for fixed energy and momentum ($E = 0.2083$ GeV ,$p = 0.1667$ GeV/c) as a function of the density. We see that a linear scaling can be applied up to $\rho = 0.8$ fm^{-3}. For higher densities we observe the mentioned saturation.

Figure 2.16 shows the on-shell width Γ_{on} as a function of the density for fixed energies. The black solid line shows the result of our calculation for the energy $E = 83$ MeV that is always above the Fermi energy and not in the vicinity of the valley around the Fermi energy. The dashed line shows the result for the energy $E = -58$ MeV that is below the Fermi energy and not in the vicinity of the valley around the Fermi energy. For both energies we observe a linear density dependence. However, the slope is bigger for the energy above the Fermi energy. The linear dependence can be applied up to densities between 0.7 fm^{-3} and 0.8 fm^{-3} that we also observed for the width with fixed energy and momentum in figure 2.15.

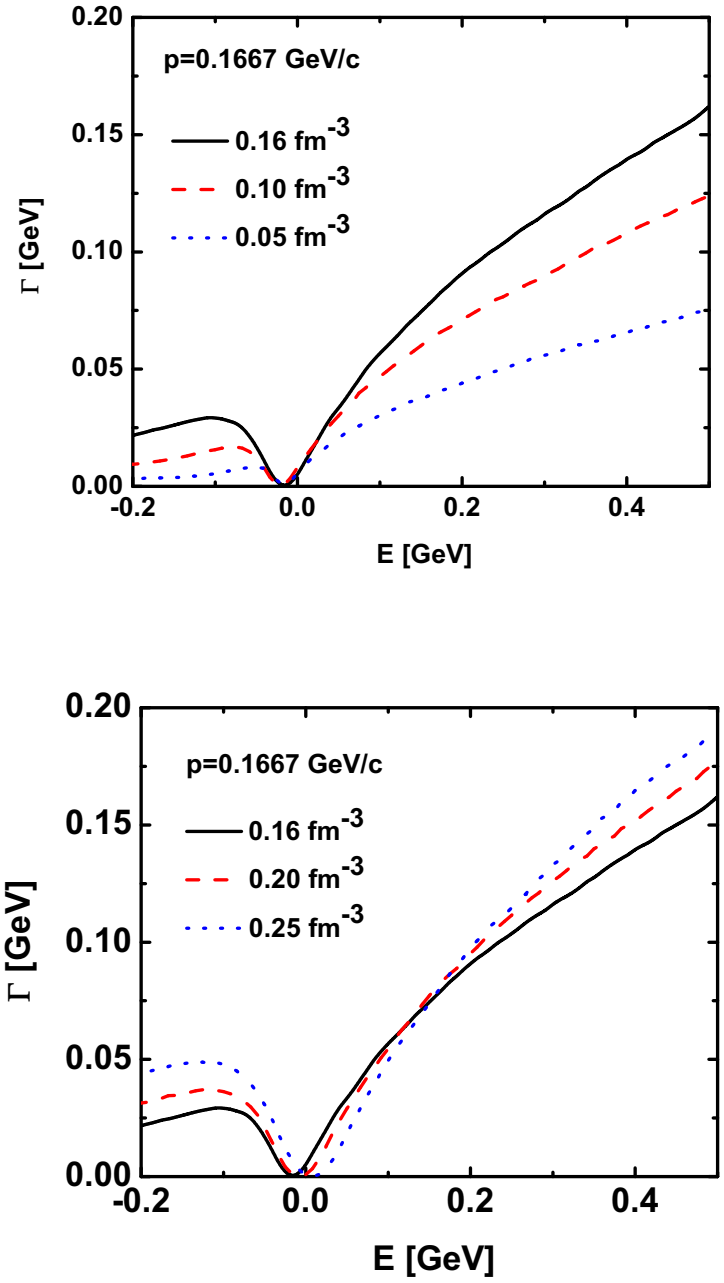

Figure 2.14: Self-consistently calculated width as a function of the energy E for fixed momentum $p = 0.1667$ GeV/c for different densities.

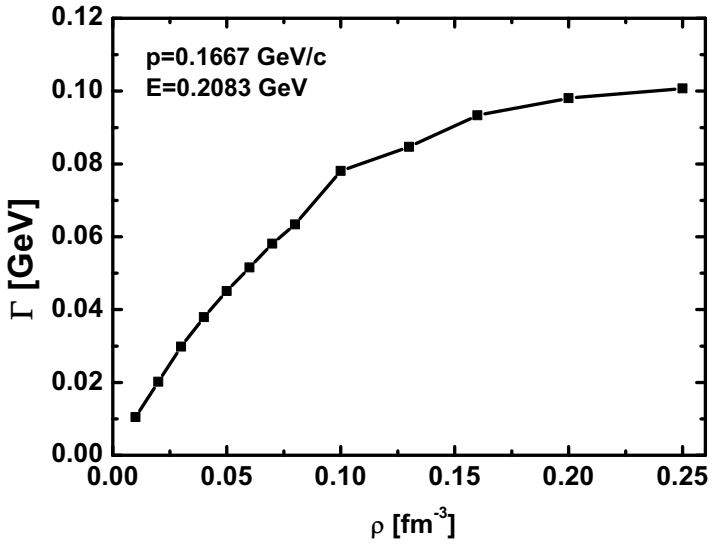

Figure 2.15: Self-consistently calculated width, including the dispersive part of the self-energy, at fixed energy $E = 0.2083$ GeV and fixed momentum $p = 0.1667$ GeV/c as a function of the density.

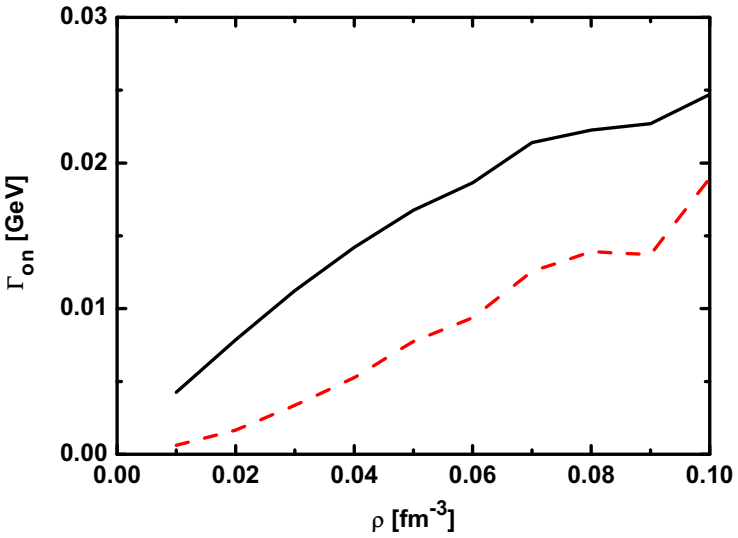

Figure 2.16: The on-shell width $\Gamma_{on}(E)$ as a function of the density at fixed energy. The solid black line shows the result of our calculation for the energy $E = 83$ MeV that is above the Fermi energy for all densities and not in the vicinity of the valley around the Fermi energy, the dashed line for the energy $E = -58$ MeV below the Fermi energy and not in the vicinity of the valley around the Fermi energy.

2.7 Momentum Distribution

The momentum distribution yields the probability to find a particle with a given momentum. At zero temperature, the states of the spectral function are filled up to the Fermi energy ω_F. Thus we can calculate the momentum distribution from [Dic05]

$$n(\vec{p}) = \frac{1}{2\pi} \int_{-\infty}^{\omega_F} d\omega \; \mathcal{A}(\vec{p}, \omega) \; . \tag{2.77}$$

Assuming a constant width in equation (2.77) yields

$$\begin{aligned} n(\vec{p}) &= \int_{-\infty}^{\omega_F} d\omega \; \frac{\Gamma}{(\omega - \omega_{\vec{p}})^2 + \frac{\Gamma^2}{4}} \\ &= \frac{1}{\pi} \int_{-\infty}^{2\frac{\omega_F - \omega_{\vec{p}}}{\Gamma}} d\xi \; \frac{1}{\xi^2 + 1} \\ &= \frac{1}{\pi} \arctan\left(2\frac{\omega_F - \omega_{\vec{p}}}{\Gamma}\right) + \frac{1}{2} \end{aligned}$$

The function $\arctan(x)$ has values between $-\frac{\pi}{2}$ and $\frac{\pi}{2}$. At $x = 0$ the function is zero. For negative x the function is negative and reaches $-\frac{\pi}{2}$ very fast. For positive x the function is positive and reaches $\frac{\pi}{2}$ very fast. Hence $\omega_F - \omega_{\vec{p}}$ determines the sign of the function and Γ determines the size of the transition region. In the limit $\Gamma \to 0$ the function has the value $\frac{\pi}{2}$ for $\omega_{\vec{p}} < \omega_F$ and $-\frac{\pi}{2}$ for $\omega_{\vec{p}} > \omega_F$ such that we obtain the step function known from the free Fermi gas.

The dashed curve in figure 2.17 shows the distribution function calculated with a constant width of 6 MeV at $\rho = 0.16$ fm^{-3}. We see that the states below the Fermi momentum are filled to 98%. The transition region around the Fermi momentum is about $p = 0.21$ GeV/c and $p = 0.30$ GeV/c.

Now we take a look at the distribution function coming from the self-consistent calculation. The solid line in figure 2.17 shows the momentum distribution using the self-consistently calculated width from section 2.6 at $\rho = 0.16$ fm^{-3}, including the real part of the self-energy. Below the Fermi momentum the distribution function is almost constant at about 0.89 and lower than the distribution function with the constant width. We see that there is a sharp drop at the Fermi momentum. This is due to the fact that the width is zero at the quasi particle peak for $\omega_{\vec{p}} = \omega_F$. The wiggles and the kink at $\omega = \omega_F$ of the self-consistent calculation are due to the numerical integration over the sharp quasi-elastic peak near ω_F. Above the Fermi momentum we see that there are more states populated in the case of the constant width.

The momentum distribution of the self-consistent calculation has a unique shape. It cannot be reproduced by a simple constant width. For the population

of the high momentum tail one needs a rather big width but for the sharp drop near the Fermi momentum one needs a small width. So even if a constant width was reasonable for scattering processes it is not be suitable for the momentum distribution and therefore it is not be suitable for the initialization of the nucleus.

Next we want to know the density of the system. The density can be calculated from the momentum distribution: We consider the integral

$$\begin{aligned} I(p) &= g \int d^3p' \; n(p')_{|_{p'<p}} \\ &= g \frac{1}{2\pi^2} \int_0^p dp' \; p'^2 n(p') \; , \end{aligned} \tag{2.78}$$

where g is the degeneracy of the state. In our calculation the degeneracy is four (spin$\times$ isospin). The density is given by

$$\rho = I(\infty) \; .$$

Figure 2.17 shows the function (2.78) as a function of the momentum. The black solid line shows the result of the calculation performed with the self-consistently calculated width from section 2.6 at $\rho = 0.16$ fm^{-3}. Below the Fermi momentum $p_F = 0.27$ GeV/c the function increases proportional to the momentum cubed because the momentum distribution is almost constant below the Fermi momentum. At the Fermi momentum it reaches the value $I(p_F) = 0.145$fm^{-3}. Above the Fermi momentum the functions grows slowly, at the momentum $p = 0.8$ GeV/c the function has the value $I(0.8 \text{ GeV}/c) = 0.184$fm^{-3} and at the momentum $p = 1.2$ GeV/c the function has the value $I(1.2 \text{ GeV}/c) = 0.187$ fm^{-3} and saturates in this region.

The dashed line shows the result of the calculation performed with the constant width of $\Gamma = 6$ MeV. Again we observe an increase proportional to the momentum cubed below the Fermi momentum. As we see in figure 2.17 the momentum distribution of the calculation performed with the constant width is higher below the Fermi momentum. Therefore, the value of $I(p)$ is higher at the Fermi momentum than for the calculation performed with the self-consistent width. However, the difference between the two results at the Fermi momentum is not as big as one would expect naively ($\Delta I(p_F) \approx 0.05$fm^{-3}). This is due to the weight p^2, coming from the integral in equation 2.78, so that higher momenta have a bigger influence than lower momenta. The increase above the Fermi momentum is lower than in the case of the self-consistent result. The two curves intersect at about $p = 0.479$ GeV/c. The calculation for the constant width has the value 0.177 fm^{-3} at the momentum $p = 0.8$ GeV and is below the result performed with the self-consistent width ($I = 0.184$ fm^{-3}).

In both results we observe that the calculated density is above the initial density. The Fermi momentum was determined assuming quasi-particles, i.e. a step function as momentum distribution. Including the collision terms from section

2.3.2 into the self-energy yields a momentum distribution that differs from the step function (See figure 2.17). However, the Fermi momentum and the corresponding Fermi energy is still the same as in the mean-field approximation. Therefore, the new density differs from the initial one. Furthermore, the Skyrme potential is calculated using the mean-field approximation , i.e. the step function as momentum distribution, and using the initial density. The increase of the density can be explained physically. We start with the ground state of the mean-field approximation. Including the collision terms the states broaden in the energy direction so that we can lower the total energy per nucleon if we fill up all states up to the Fermi energy regardless of their momenta. As we see in figure 2.17 we can put more particles into the ground state than in the pure mean-field approximation such that the density increases and the total energy per nucleon decreases. In other words we do not fix the density but the Fermi energy. However, it would be better to fix the density. To do this, we have to determine numerically the Fermi momentum and the Fermi energy after each iteration. Furthermore, the potential parameters are fitted assuming the mean-field potential. Therefore, one has to consider how the Skyrme parametrization should be modified.

Up to now we have considered only the width, i.e. the imaginary part of the self-energy. Usually, the imaginary part of the self-energy determines the shape of the spectral function and the real part determines the location of the quasi elastic peak. At momenta near the Fermi momentum we have to consider the real part of the self-energy because the width near the quasi particle peak is small compared to the real part of the self-energy. Figure 2.19 shows cuts through the calculated width at fixed momenta. The chosen momenta are around p_F. The calculation has been performed for the density $\rho_0 = 0.16$ fm^{-3}. We see that the width has its minimum at ω_F. In fact, the width at ω_F is zero at zero temperature. It has to be zero by definition because the ground state is stable. Thus, we can parametrize the width around p_F and ω_F with

$$\Gamma \approx a(|\vec{p}|)\ (\omega - \omega_F)^2\ . \tag{2.79}$$

Figure 2.20 shows a cut through the corresponding real part of the self-energy without the mean field part at $p = 0.23$ GeV/c. Near ω_F we can approximate the real part of the self-energy with

$$\text{Re}\ \Sigma(\omega, \vec{p}) \approx -b(\vec{p})(\omega - \omega_F)\ . \tag{2.80}$$

Using equations (2.79) and (2.80) in the spectral function for $p = p_F$ yield

$$\begin{aligned} \mathcal{A}(p_F, \omega) &= \frac{a\xi^2}{((1+b)\xi)^2 + \frac{a^2\xi^4}{4}} \\ \mathcal{A}(p_F, \omega) &= \frac{a}{(1+b)^2 + + \frac{a^2}{4}\xi^2}\ , \end{aligned} \tag{2.81}$$

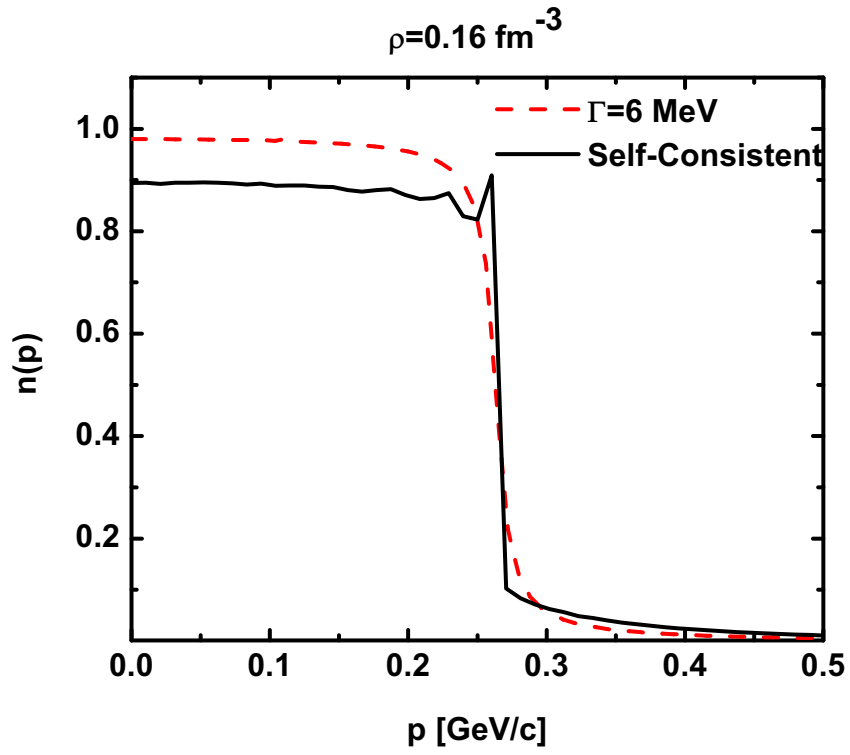

Figure 2.17: Comparison between the momentum distribution calculated with a constant width of $\Gamma = 6$ MeV and the momentum distribution calculated with Re Σ and Im Σ from a self-consistent calculation at $\rho = 0.16\text{fm}^{-3}$

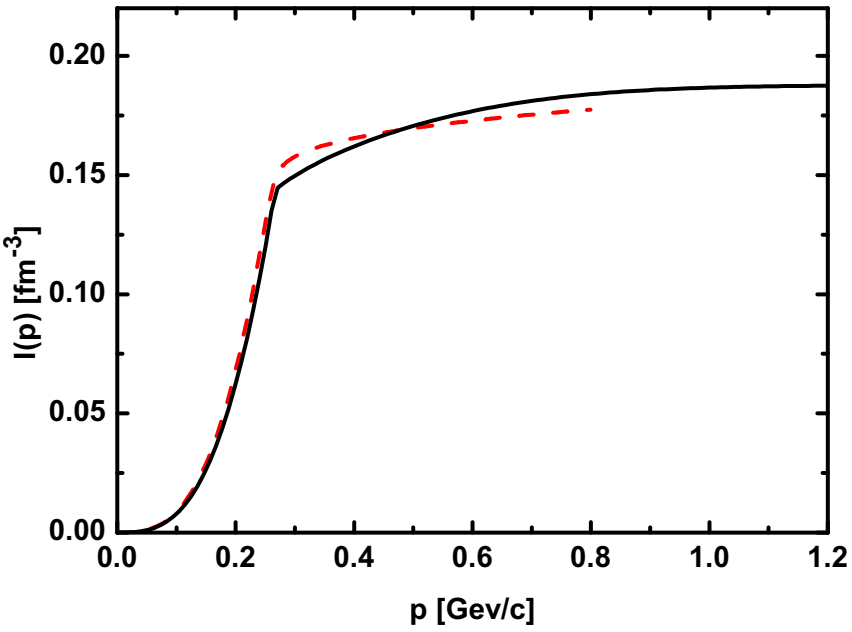

Figure 2.18: Integration of the momentum distribution as a function of the upper limit p (function (2.78)). The solid black line shows the result of the calculation using the self-consistently calculated width for the initial density $\rho = 0.16$ fm^{-3}, the dotted line the result of the calculation using the constant width of 6 MeV.

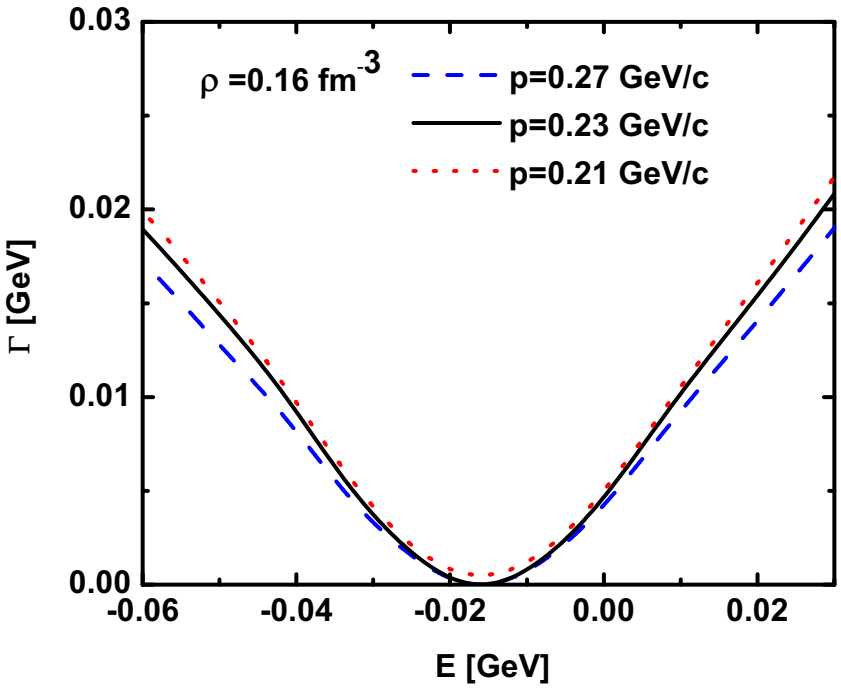

Figure 2.19: Self-consistently calculated width near p_f as a function of the energy at the density $\rho = 0.16\text{fm}^{-3}$. The dashed line shows the width at fixed momentum $p = 0.21$ GeV/c, the black solid line the width at fixed momentum $p = 0.23$ GeV/c, the dashed line the width at fixed momentum $p = 0.27$ GeV/c.

with $\xi = \omega - \omega_F$. We see that even when the width goes to zero the spectral functions remains finite due to the dispersive real part of the self-energy. Using expression (2.81) we can calculate the momentum distribution function at the Fermi momentum

$$n(p_F) \quad = \quad \frac{1}{2}\frac{1}{1+b} \; . \tag{2.82}$$

We can see that the momentum distribution at $p = p_F$ is determined by the slope of the real part of the self-energy. Since $b > 0$, it reduces the value at the Fermi momentum. Hence, a calculation without the real part of the self-energy overestimates the momentum distribution around the Fermi momentum.

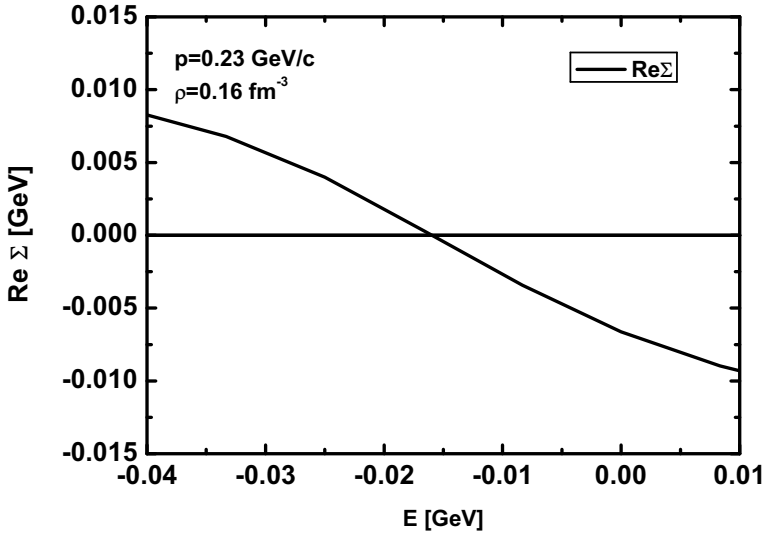

Figure 2.20: Re Σ near p_f and ω_F without Σ_{HF} as a function of the energy at fixed momentum $p = 0.23$ GeV/c.

3 BUU Model

In classical statistical dynamics transport processes are described by the Boltzmann equation. Nordheim, Uehling and Uhlenbeck derived a quantum mechanical extension that can be used for fermionic systems, the "Boltzman-Uehling-Uhlenbeck equation" (BUU).

In the late 80's the theory group at the JLU Giessen started to use the BUU model to describe heavy-ion collisions and later on also photon, pion, electron and neutrino induced processes. The present work is based upon the model version described at the project homepage [GiB].

3.1 Mean Field Potential

The pole of the spectral function is determined by the real part of the self energy. Within GiBUU the mean field self-energy is parametrized by a density dependent Skyrme part and an additional momentum dependent part ([WPKG88],[GWP$^+$90]):

$$U(\vec{r},\vec{p}) = A\frac{\rho(\vec{r})}{\rho_0} + B\left(\frac{\rho(\vec{r})}{\rho_0}\right)^{\tau} + \frac{2C}{\rho_0} g \int \frac{d^3p'}{(2\pi)^3} \frac{n(\vec{r},\vec{p}\,')}{1+(\frac{\vec{p}-\vec{p}'}{\Lambda})^2} \ . \tag{3.1}$$

However, this potential differs from the potential in chapter 2. We will solve this problem in chapter 4.

The ground state of our model is given by

$$n(\vec{r},\vec{p}) = \theta(p_f(\vec{r}) - |\vec{p}|) \ . \tag{3.2}$$

Using equation (3.2) we can calculate the integral in (3.1) analytically

$$\begin{aligned} \frac{2C}{\rho_0} g \int \frac{d^3p'}{(2\pi)^3} \frac{n(\vec{r},\vec{p}')}{1+(\frac{\vec{p}-\vec{p}'}{\Lambda})^2} &= \\ &= \frac{\Lambda^3}{8\pi^2}\left[\frac{p_f^2(\vec{r})+\Lambda^2-p^2}{2p\Lambda}\ln\left(\frac{(p+p_f(\vec{r}))^2+\Lambda^2}{(p-p_f(\vec{r}))^2+\Lambda^2}\right) + \frac{2p_f(\vec{r})}{\Lambda}\right. \\ &\quad \left. -2\left(\arctan\left(\frac{p+p_f(\vec{r})}{\Lambda}\right) - \arctan\left(\frac{p-p_f(\vec{r})}{\Lambda}\right)\right)\right] . \end{aligned} \tag{3.3}$$

The parameters A, B, C, τ, Λ are fitted to nuclear matter data. For further information see [Tei99].

K[MeV]	A[MeV]	B[MeV]	C[MeV]	τ	Λ[fm^{-1}]
290	-29.3	57.2	-63.5	1.76	2.13

Table 3.1: Mean field parameters from [Tei99]

With the energy density we can calculate the equation of state (EOS), the binding energy per nucleon. The parameters are fixed such that the binding energy per nucleon has its minimum at ρ_0 [Tei99],

$$\begin{aligned} \frac{\partial}{\partial\rho}\frac{E}{A}_{|\rho=\rho_0} &= 0 \\ \frac{E}{A}_{|\rho=\rho_0} &= -16 \text{ MeV} . \end{aligned}$$

The compressibility K of the EOS is the curvature of the EOS with respect to the density

$$9\rho\frac{\partial^2}{\partial\rho^2}\frac{E}{A}_{|\rho=\rho_0} = K .$$

For the density dependent part we require ([WPKG88],[GWP$^+$90])

$$\begin{aligned} U(p=0,\rho_0) &= -75 \text{ MeV} \\ U(p=800 \text{ MeV},\rho_0) &= 0 \\ U(p=\infty,\rho_0) &= 30.5 \text{ MeV} . \end{aligned}$$

In the following calculations we use the medium momentum dependent dependent EOS [Tei99]. Table 3.1 shows the parameters for the medium momentum dependent equation of state.

Figure 3.1 shows the potential U for different scenarios of $\frac{\rho}{\rho_0}$ as a function of $|\vec{p}|$.

3.2 Scalar Potential

The relativistic Hamiltonian in GiBUU has within the local rest frame the form

$$H = \sqrt{(m_N + U_S)^2 + \vec{p}^2} + V_0(\vec{r},\vec{p}) , \tag{3.4}$$

with the potential zeroth component of the vector potential $V_0(\vec{r},\vec{p})$ and the scalar potential U_S. The spatial parts of the vector potential are zero in the local rest frame.

Due to numerical reasons we use only a scalar potential so that we do not have to boost the mean field potential in the particular calculation frame. Therefore

we set $V_0(\vec{r}, \vec{p})$ to zero and include the mean field potential in the scalar potential. The scalar potential is given by

$$U_S = \sqrt{(\sqrt{m_N^2 + \vec{p}_{\mathrm{LRF}}^2} + U(\rho, \vec{p}_{\mathrm{LRF}}))^2 - \vec{p}_{\mathrm{LRF}}^2} - m_N \ , \tag{3.5}$$

and we obtain effective mass of the nucleon by

$$m_{eff} = m_N + U_S \ . \tag{3.6}$$

For off-shell particles we replace the bare mass m_N with the off-shell mass μ in equation (3.4) and (3.5).

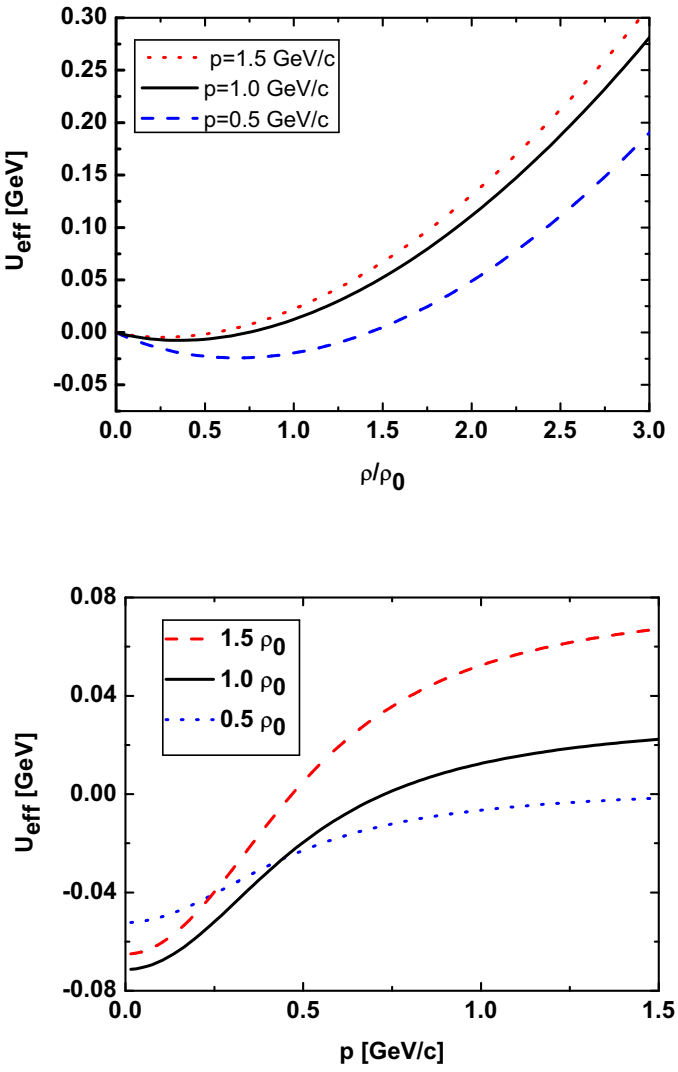

Figure 3.1: Momentum dependent potential (3.1), in ρ and in p direction

4 Numerical Realization

4.1 Initialization of the Nucleus

4.1.1 Local Density Approximation

Until now we assumed nuclear matter, i.e. an infinite medium. The real nucleus has a finite size. Therefore surface effects and other boundary conditions have influence on its properties.

We take this into account by applying the local density approximation (LDA). We assume that we can locally approximate the nucleus by nuclear matter. The momentum distribution function for the nucleus is given by

$$n_A(p) = \int d^3r \; n(\vec{r}, \vec{p}) \; ,$$

where $n(\vec{r}, \vec{p})$ is the momentum distribution calculated for nuclear matter for the local density at $\vec{r}$. We use a parametrization for the local momentum distribution function [Leh03]. For $\rho = \rho_0 = 0.168$ fm^{-3} the momentum distribution is given by

$$n(p, \rho_0) = \begin{cases} v_1 & \text{for } p < p_F \\ v_2 \frac{\exp(-A\ p)}{p^2} & \text{for } p > p_F \end{cases} \tag{4.1}$$

with the Fermi momentum

$$p_F(\rho(\vec{r})) = \left(\frac{6\pi^2}{4} \rho \right)^{\frac{1}{3}} \; .$$

Table 4.1 shows parameters for $\rho = \rho_0$. They are fitted to the momentum distribution in [Leh03] of nucleons in nuclei.

ρ	v_1	v_2	A [1/ GeV]
0.168	0.85	0.15	2.3

Table 4.1: Parameters for the parametrized momentum distribution function (4.1). The parameters are fitted to the momentum distribution used in [Leh03].

v_1	v_2	A [1/ GeV]	a	b
0.83	0.24	3.67	-0.03	0.27

Table 4.2: Parameters for the parametrized momentum distribution function (4.1) and (4.2) . The parameters are fitted to the momentum distribution used in chapter 2.

The step in the momentum distribution is always at the Fermi momentum. Thus the step is a function of the density. Replacing the momentum with

$$\tilde{p} \equiv p\left(\frac{\rho}{\rho_0}\right)^{\frac{1}{3}} .$$

yields a density independent Fermi momentum. With the new momentum scale we can use the parametrized density dependent momentum distribution

$$n(\tilde{p},\rho) = n(\tilde{p},\rho_0)\begin{cases}(\frac{\rho}{\rho_0})^a & \text{for } \tilde{p} < p_F(\rho_0)\\ (\frac{\rho}{\rho_0})^b & \text{for } \tilde{p} > p_F(\rho_0)\end{cases} . \tag{4.2}$$

The parameters are fitted at $p^2 f(\tilde{p})$ for different densities [Leh03]: $a = -0.04$ $b = 0.34$. We see that the bulk part, i.e. the momentum distribution below the Fermi momentum, is almost constant. However the high momentum tail above the Fermi momentum increases for higher densities.

Since the momentum distribution of Lehr [Leh03] differs from the momentum distribution in chapter 2 we fit the parameters on the momentum distribution of chapter 2. The parameters are shown in table 4.2. We see that we almost obtain the same result for the bulk part as in the parametrization on the Lehr results. The tail is higher but the decreasing is faster. Furthermore we observe a smaller density dependence. In section 5.6 we will see that the difference between these two parametrizations has almost no influence on the inclusive cross sections, i.e. the results are almost the same for both parametrizations. The most calculations are done with the parametrization of the momentum distribution of Lehr. However this can change if one uses the spectral function for the initialization of the nuclei and not only the momentum distribution.

4.1.2 Density Profile

In order to get a real nucleus we have to distribute the nucleons in coordinate space. Later we use the local density approximation (LDA) for the momentum distribution.

For light nuclei up to O^{18} we use a harmonic oscillator type density parametrization

$$\rho_{A\leq 18}(\vec{r}) = \rho_0 \left(1 + a\left(\frac{r}{R}\right)^2\right)\exp\left(-\frac{r}{R}\right) . \tag{4.3}$$

Nucleus	$R_{p,e}$ [fm]	$a_{p,e}$ [fm]	$R_{n,e}$ [fm]	$a_{n,e}$ [fm]
${}^{16}_{8}O$	1.833	1.544	1.815	1.529

Table 4.3: Proton and neutron matter density parameters for the density profile (4.3) taken from [NOGR93]

The parameters for the proton densities are based on the compilation of [NOGR93] from electron scattering. The neutron densities are provided by Hartree-Fock calculations. Table 4.3 shows proton and neutron matter density parameters for ${}^{16}_{8}O$.

4.1.3 Mass and Energy Determination

After we have determined the momentum of the nucleon, we have to determine its energy. As we know from section 2.7, the momentum distribution function can be calculated from the spectral function[1] in nuclear matter

$$n(p) = \frac{1}{2\pi} \int_{-\infty}^{\omega_F} d\omega \; \mathcal{A}(\omega, \vec{p}) \; .$$

For $|\vec{p}| < p_F$ the pole of the spectral function is located within the integration limits. Thus, most of the baryons below p_F are peaked around the on-shell peak of the spectral function. Moreover, we have seen in chapter 2 that the width below the Fermi energy is small and thus the on-shell peak is high and narrow . Therefore we treat particles below p_F as on-shell particles.

The situation changes for $|\vec{p}| > p_F$. Since the states above p_F are only filled up to ω_F the highest energy of any bound state is ω_F. Hence, there are no on-shell particles in the high momentum tail. As an approximation we assign the energy ω_F to all particles with momenta $p > p_F$. The Fermi energy is chosen to be the binding energy per nucleon and therefore the total energy of the nucleus is in the desired region. This method has the numerical advantage that we do not have to distribute the particles in energy direction that would require the inverse of the spectral function for the numerical routines.

Taking into account off-shell particles and a momentum dependent mean field we have to determine the masses of the particles. To do so we have to solve the following equation for m:

$$p_0 \;\; = \;\; \sqrt{\vec{p}^{\,2}_{LRF} + m^2} + U(\vec{p}_{LRF}, \rho(\vec{x}))$$

where $U(\vec{p}_{LRF}, \rho(\vec{x}))$ is the mean field potential (3.1).

[1] Here we use the relativistic energy. Usually the Fermi energy does not include the mass of the particle. Therefore we have to shift the energy $\omega \to \omega + m$. The integral stays the same.

It can happen that the mass squared becomes negative, i.e. the particle is faster than light. Since we have off-shell particles the energy and the momentum are not strictly related. So we can have states with a momentum that is greater than the energy and thus a negative squared mass. In quantum mechanics or special relativity particles that are faster than light are not forbidden. But those particles are a problem for our semi-classical model. Therefore, we introduce a spatial momentum cutoff. This is reasonable because the potentials and our assumptions cannot be extended to any momentum scale.

Figures 4.1 and 4.2 show the momentum and the mass distribution for $^{16}_{8}$O in arbitrary units. The calculation has been performed with a momentum cutoff at 0.8 GeV/c. In figure 4.1 we see a smooth drop in the momentum distribution instead of the sharp step that we have in nuclear matter. Due to the approximations described above, the mass distribution includes only off-shell masses coming from the high momentum tail so that we obtain only masses below the bare mass of $m = 0.938$ GeV. Through the momentum cutoff we neglect particles that have masses below 0.4 GeV.

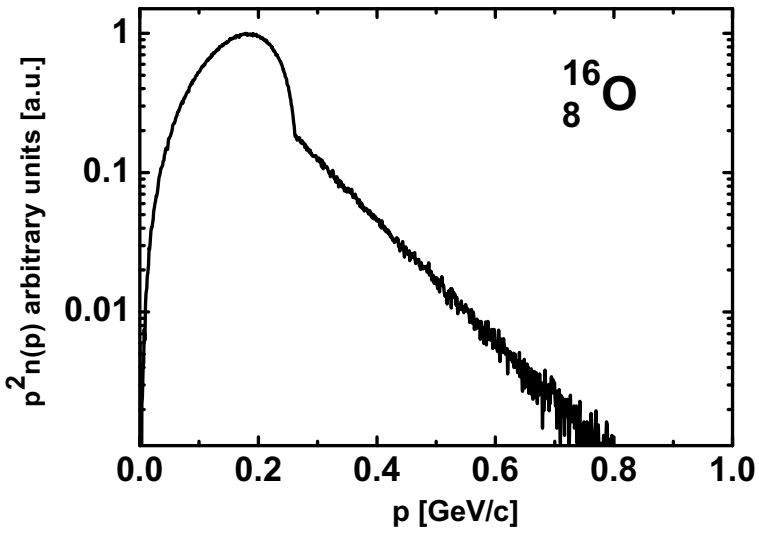

Figure 4.1: Momentum distribution for $^{16}_{8}$O with momentum cutoff at $p = 0.8$ GeV/c (in arbitrary units).

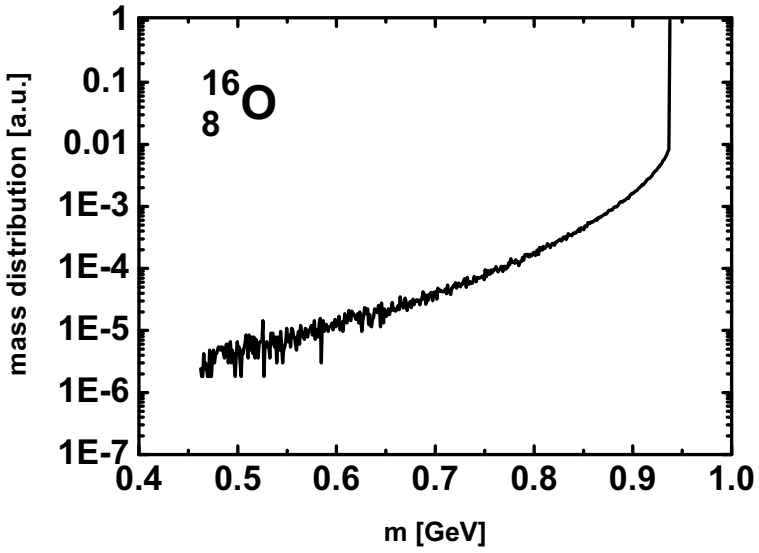

Figure 4.2: Mass distribution for $^{16}_{8}$O with momentum cutoff at $p = 0.8$ GeV/c (in arbitrary units).

4.2 Spectral Function

The spectral function used in the GiBUU code is given by

$$\mathcal{A}(|p|) \;=\; \frac{1}{\pi}\frac{|p|\;\Gamma}{(p^2-M^2)^2+p^2\Gamma^2}$$

with the invariant mass

$$|p| = \sqrt{p_\mu p^\mu}\ .$$

In order to use the self-consistently calculated width from chapter 2 in the GiBUU model the width is calculated and stored on a grid in energy, momentum and density. The interpolation between grid points in the energy momentum plane can be done with the usual interpolation routines. However, a simple interpolation between two density grid points would give a wrong value:

In figure 4.3 we see the self-consistently calculated width as a function of the energy for different densities. The densities between $\rho = 0.10$ fm^{-3} and $\rho = 0.20$ fm^{-3} are omitted because the Fermi energy has its minimum at the saturation density $\rho_0 = 0.16$ fm^{-3} so the change of the Fermi energy in density is small aroung ρ_0. The effect for low densities can be seen in figure 4.4 for the densities $\rho = 0.16$ fm^{-3} and $\rho = 0.03$ fm^{-3}. We see that the width is always zero at the

Fermi energy. The Fermi energy is a function of the density so that the null moves as a function of the density.

Let us consider the interpolation of the width at the Fermi energy. The two neighboring grid points in energy are not zero because the Fermi energy of their corresponding density differs from the interpolated one. Hence, the interpolated width at the Fermi energy is not zero.

We want to ensure that the width is zero at the Fermi energy because the ground state is stable and therefore the states at the surface has to be stable. Hence, the particle at the Fermi surface have to be stable. To do so, we introduce the shifted width

$$\tilde{\Gamma}(\omega, p) \equiv \Gamma(\omega + \omega_F(\rho), p) \ . \tag{4.4}$$

Using this shifted width means that the important quantity is the difference between the particular energy and the Fermi energy. Thus, the root of $\tilde{\Gamma}(\omega, p)$ is at $\omega = 0$ for all densities and therefore the known interpolation routines can be applied to the shifted width.

A problem can occur if one uses a self-consistently calculated width that is calculated with a different mean field than used in the GiBUU model. In particular, the self-consistently calculated width of chapter 2 is calculated with a different mean field. The Fermi energies of the two systems are not the same. Therefore we shift the energy by the difference of the Fermi energy ω_F of the GiBUU model and the Fermi energy of the calculated width ω'_F:

$$\Gamma(\omega, p) \rightarrow \Gamma(\omega - (\omega_F - \omega'_F), p) \ .$$

After that we use the interpolation routine explained above. With this routine it is possible to use widths that were not particularly calculated for the GiBUU model. Thus, we can profit of the work of many people and can compare the effect of our model. In the future it is planned to do the calculation with the same mean field as in GiBUU and it will be interesting to see how good this shift routine works.

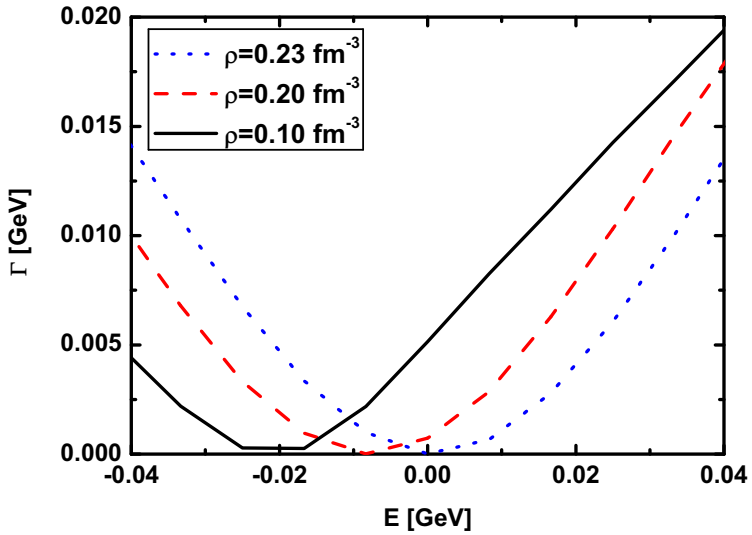

Figure 4.3: Self-consistently calculated width for different densities above ρ_0 for fixed momentum $p = 0.3125$ GeV/c:

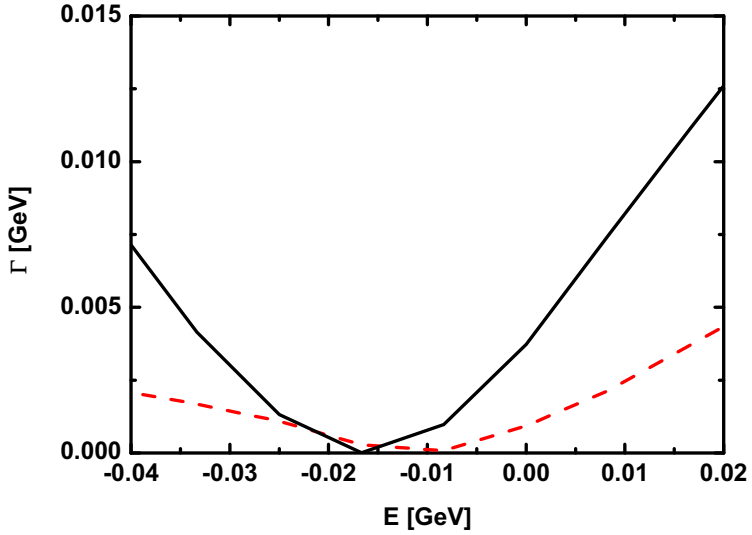

Figure 4.4: Self-consistently calculated width for densities below below ρ_0 for the fixed momentum $p = 0.3125$ GeV/c: The black solid line is the width for the density $\rho_0 = 0.16$ fm^{-3} the red dashed line is the width for the density $\rho = 0.03$ fm^{-3}

5 In Medium Cross Sections

In this chapter we will show how we modify the elementary cross sections for electron and neutrino induced reactions so that they take into account in-medium effects.

5.1 Impulse Approximation

For large enough energy transfer the nucleus is seen by the lepton as a collection of individual nucleons. Therefore we can write the cross section of the nucleus as the sum of all scatterings on the nucleons that are distributed according to the nucleon distribution function $n(\vec{r},\vec{p})$

$$\frac{d\sigma_A}{dE_{l'}d\Omega} = \int d^3r\ n(\vec{r},\vec{p})\ \frac{d\sigma_{\text{nucleon}}}{dE_{l'}d\Omega}\ .$$

5.2 In Medium Modifications of the Cross Section

In the nucleus, protons and neutrons are no free particles anymore. They interact with each other and have different properties than in vacuum. Therefore we carefully account for the collision broadening and the change of the nucleon dispersion relation.

Consider the lepton-nucleon collision (see figure 5.1)

$$l(k) + N(p) \to l'(k') + N'(p')\ , \tag{5.1}$$

with the initial state momenta $p^\mu = (E,\vec{p})$, $k^\mu = (E_l,\vec{k})$ and the final state momenta $p'^\mu = (E',\vec{p}\,')$, $k'^\mu = (E_{l'},\vec{k'})$. The double differential cross section is given by

$$\frac{d^2\sigma_{lN}}{dQ^2dE_{l'}} = \int d\phi\ \frac{1}{64\pi^2}\frac{1}{|k\cdot p|}\frac{1}{E_l}\delta(p'^2 - M'^2)\ |\bar{\mathcal{M}}|^2$$

with $Q^2 = -(p'-p)^2 = -t$, the azimuthal angle $\phi \in [0, 2\pi)$ and the invariant mass of the outgoing nucleon

$$M'^2 = E'^2 - \vec{p}'^2\ .$$

The delta-function comes from the on-shell condition of the outgoing nucleon.

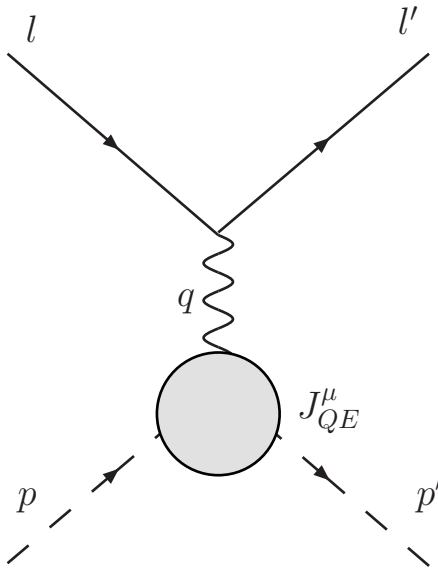

Figure 5.1: Quasi elastic lepton nucleon scattering: l is the four momenta of the incoming lepton, l' of the outgoing lepton, p of the incoming nucleon, p' of the outgoing nucleon.

For a resonance this is not true anymore. Due to a finite life time, energy and momentum can differ from the on-shell condition. The invariant mass

$$W^2 \equiv p'_\mu p'^\mu$$

is not fixed. Therefore we have to replace the delta function with the spectral function

$$\delta(p'^2 - M'^2) \rightarrow \mathcal{A}(W) = \frac{1}{\pi} \frac{W\ \Gamma}{(W^2 - M^2)^2 + W^2\Gamma^2}\ .$$

We have shown in chapter 2 how we calculate the spectral function. However, the spectral function of chapter 2 is not calculated with the mean-field used in GiBUU. Therefore, we shift the width which has been obtained in chapter 2 according to the method presented in section 4.2. In the future it is planned to use a self-consistently calculated width, which fits to the mean field potential of the GiBUU model.

Further in-medium modifications that enter the GiBUU model are the density and momentum dependent mean field, Fermi motion and Pauli blocking.

5.3 Elementary Lepton Nucleon Reaction

We proceed with the calculation of the matrix element squared $|\bar{\mathcal{M}}|^2$ for the general process defined in equation (5.1). The matrix element squared is given

by

$$|\bar{\mathcal{M}}|^2 = c\ L_{\alpha\beta}H^{\alpha\beta}\ , \tag{5.2}$$

with the coupling c, the leptonic tensor $L_{\alpha\beta}$ and the hadronic tensor $H^{\alpha\beta}$. The coupling c depends on the particular process. We are interested in neutrino induced charged current (CC) reactions and in electron induced electromagnetic interactions (EM):

$$c_{CC} = \frac{G_F^2 cos\theta_C}{2} \tag{5.3}$$

$$c_{EM} = \frac{e^2}{q^4}\ . \tag{5.4}$$

The leptonic tensor is given by

$$L_{\alpha\beta} = \frac{1}{n_s}\mathrm{Tr}\ [(\not{k} + m_l)\gamma_\alpha(1 - a\gamma_5)(\not{k}' + m_{l'})\gamma_\beta(1 - a\gamma_5)] \tag{5.5}$$

where m_l is the mass of the incoming lepton, and $m_{l'}$ the mass of the outgoing lepton. For electromagnetic interactions a is set to zero, for charged current interactions one sets $a = 1$. The factor n_s denotes the number of possible initial state spins, i.e. $n_s = 1$ for neutrinos and $n_s = 2$ for electrons.

In this work, we concentrate on quasi-elastic processes, i.e. $\nu n \rightarrow l^- p$ for neutrino induced reactions. Due to charge conservation there is no quasi elastic process with neutrinos on protons. For electron induced reactions we have the possible reactions $ep \rightarrow ep$ and $en \rightarrow en$. However, there are also contributions from resonance production and background.

5.4 Quasi Elastic Scattering

In view of the fact that current QCD calculations cannot produce hadronic vertices, we have to use an explicit parametrization for the hadronic current of the quasi elastic reaction based on general assumptions.

The hadronic current can be expressed as

$$\begin{aligned} J_\alpha^{QE} &= \langle N'|J_\alpha^{QE}(0)|N\rangle \\ &= \bar{u}(p')A_\alpha u(p) \end{aligned} \tag{5.6}$$

with

$$A_\alpha = (\gamma_\alpha - \frac{\not{q} q_\alpha}{q^2})F_1^V + \frac{i}{2M_N}\sigma_{\alpha\beta}q^\beta F_2^V + \gamma_\alpha\gamma_5 F_A + \frac{q_\alpha}{M_N}\gamma_5 F_P\ . \tag{5.7}$$

with M_N being the nucleon mass, $F_{1,2}^V$ the vector form factors, F_A and F_P the axial and pseudo scalar form factors which are zero in the case of EM scattering. The term $\frac{\not{q} q_\alpha}{q^2}$ takes care that the vector part of the current is conserved even for non-equal masses of the incoming and outgoing nucleon that are possible due to the momentum dependent mean field and momentum dependent mass. In our model, we use a charge averaged nucleon bare mass $M_N = 0.938$ GeV.

The vector form factors are given by

$$\begin{aligned} \text{EM: } F_{1,2}^V &= F_{1,2}^p \\ &\quad \text{for } e\ p \to e\ p\ , \\ F_{1,2}^V &= F_{1,2}^n \\ &\quad \text{for } e\ n \to e\ n, \end{aligned}$$

$$\text{CC: } F_{1,2}^V = F_{1,2}^p - F_{1,2}^n\ .$$

The Pauli form factor $F_1^{n,p}$ and the Dirac form factor $F_2^{n,p}$ can be expressed in terms of the charge and magnetic moments of the proton and the neutron

$$F_1^{n,p}(Q^2) = \left[G_E^{p,n} + \frac{Q^2}{4M_N^2} G_M^p\right] \left[1 + \frac{Q^2}{4M_N^2}\right]^{-1}\ , \tag{5.8}$$

$$F_2^{n,p}(Q^2) = \left[G_M^{p,n} - G_E^{p,n}\right] \left[1 + \frac{Q^2}{4M_N^2}\right]^{-1}\ , \tag{5.9}$$

with the so called Sachs form factors $G_E^{p,n}$ and $G_M^{p,n}$. We will use the so called BBBA05 parametrization [BBBA06]

The hadronic tensor for quasi elastic scattering is given by

$$H_{QE}^{\alpha\beta} = \frac{1}{2}\text{Tr}\ [(\not{p} + M)\tilde{A}^\alpha(\not{p}' + M')A^\beta] \tag{5.10}$$

with

$$\tilde{A}_\alpha = \gamma_0 A_\alpha^\dagger \gamma_0\ . \tag{5.11}$$

For neutrino scattering, we, in addition, need the axial form factor. Assuming pion pole dominance, we can use the partially conserved axial current hypothesis (PCAC) to relate F_A and F_P

$$F_P(Q^2) = \frac{2M_N}{Q^2 + m_\pi^2} F_A(Q^2)\ .$$

The axial form factor is given by the standard dipole form

$$F_A(Q^2) = g_A \left(1 + \frac{Q^2}{M_A^2}\right)^{-2} \tag{5.12}$$

with $g_A = -1.267$ obtained from β decay and the axial mass $M_A = 1.00$ GeV [BBA03].

5.5 Results for Electron Scattering

We shall now apply our model to electron induced QE scattering and compare our calculation to existing measurements.

Figure 5.2 shows a comparison of different calculations and data obtained by Anghinolfi et al. [A$^+$96] at a beam energy of 700 MeV and $\theta = 32°$ for the double differential cross section as a function of the energy transfer $\nu = E_l - E_{l'}$. In vacuum, the quasi-elastic peak is at

$$\nu^{QE} = \frac{Q^2}{2M} \approx \frac{E_l^2}{M}(1 - cos\theta_{lab}) \ ,$$

with E_l the beam energy and θ_{lab} the scattering angle of the outgoing electron. With the above kinematics this gives $E_\gamma^{QE} = 79$ MeV.

The dashed curve shows the result of the calculation performed with a sharp particle ($\Gamma = 1$ MeV for numerical reasons) as outgoing nucleon and with a Fermi step function in nuclear matter, but using the local density approximation (LDA). We see that this calculation overestimates the quasi-elastic peak. The peak is at about 90 $nb/(sr$ MeV) but the data has the peak at about 60 $nb/(sr$ MeV). Furthermore the measured cross section is broader than the calculated one and, in particular, peaks at a lower ν.

The dash-dotted line shows the calculation performed with the self-consistently calculated width in chapter 2 and a local Fermi step function for the LDA. We see that the width reduces the height and broadens the peak. This shows that at low momentum transfer ($Q_{QE}(700$ MeV$) \approx 385$ MeV) short-range nucleon-nucleon correlations have an influence on the inclusive double differential quasi-elastic cross section. Hence, the two-particle one-hole excitations and the one-particle two-hole excitations that are included in the self-consistently calculated width improve the description of the nucleons in our model.

The dotted curve shows the result of the calculation using the low-density parametrization, used in [BLARM07], of the collision width

$$\Gamma = \int n(p)\ \sigma(E, \vec{p}, \vec{p}\,')\ \rho\ v_{rel}\ P_{PB}\ d^3p' \ , \tag{5.13}$$

where $n(p)$ is the momentum distribution of the nucleons in the Fermi sea, $\sigma(E, \vec{p}, \vec{p}')$ the total cross section for the scattering of the outgoing nucleon with a nucleon of momentum $\vec{p}\,'$ in the vacuum, v_{rel} the relative velocity of the particle and the nucleon, and P_{PB} the Pauli blocking factor for the final state particles [BLARM07]. The total cross sections are chosen according to the GiBUU collision term [GiB] (Further details of the collision term can be found in [Leh03]). Additionally, the calculation uses locally a Fermi step function for the LDA. We see that we obtain a result that is lower than for the self-consistently calculated width (dash-dotted line).

The solid curve shows the result of the calculation performed with the self-consistent width calculated in chapter 2 and the modification of the initial nucleon from chapter 4. We see that the inclusion of the high momentum tail further reduces the height and broadens the peak. We see that we obtain almost the same result as for the result performed with the low-density parametrization (dotted line). This shows that at low momentum transfer (Q^2(700 MeV) $\approx$ 0.145 GeV^2 at the vacuum QE peak) short-range nucleon-nucleon correlations and the momentum distribution of the nucleus have an influence on the inclusive double differential quasi-elastic cross section.

Since the cross section is for low momentum transfer sensitive to Fermi motion we conclude that the remaining discrepancy of the lowest energy (wrong peak position) must be due to the momentum distribution of the nuclei and not to the spectral function.

Figures 5.3 and 5.4 show that the calculations performed with the sharp outgoing nucleon is slightly above the data for higher energies. However, the difference between this calculation and the data is smaller than for the beam energy of 700 MeV. That is due to the fact that the quasi-elastic peak is at higher momentum transfer so that the elementary cross section is not so sensitive to in-medium effects anymore. We see that the calculations using the low density approximation (dotted line) and the calculation using the self-consistently calculated width (dash-dotted line) give almost the same result. In particular, for the beam energy of 880 MeV both calculations have the same peak value. Additionally, these two calculations are closer to data than the other calculations. The calculation using the self-consistently calculated width of chapter 2 and the parametrization of the momentum distribution of chapter 4 is below the data near the quasi-elastic peak for higher energies, in particular for the beam energies of 1200 MeV and 1500 MeV. Furthermore, we see that for higher beam energies at energy transfers above the quasi-elastic peak more processes play a major role.

Since the results of the calculation using the collision width and the calculation using the self-consistently width are at all beam energies almost the same, we take a closer look at these widths. In figure 5.5 we see the on-shell width as a function of the momentum for the density $\rho = 0.14\text{fm}^{-3}$. The dashed line shows the on-shell width for the low-density width parametrization (5.13), using the GiBUU collision term. We see that the function is zero up to the Fermi momentum at about $p = 0.25$ GeV/c. Between $p = 0.25$ GeV/c and $p = 0.48$ GeV/c the width increases rapidly. Above $p = 0.48$ GeV/c the increase is smaller. At $p = 0.8$ GeV/c the width has the value of $\Gamma = 0.041$ GeV.

The solid line shows the on-shell width for the self-consistently calculated width of chapter 2. The width starts at zero momentum at the value of $\Gamma = 0.018$ GeV. At about $p = 0.25$ GeV/c we find the minimum of the width at the Fermi momentum. Above the Fermi momentum the width increases and is almost the same like the low-density parametrization but below it. With increasing energy the slope of the width decreases. At about $p = 0.61$ GeV/c the both widths in-

tersect and above this energy the self-consistently calculated width is above the low-density parametrization. At $p = 0.8$ GeV/c it has the value $\Gamma = 0.050$ GeV. The wiggles in both curves are due to the interpolation routines.

Between about $p = 0.20$ GeV/c and about $p = 0.60$ GeV/c both widths are nearly the same. Therefore, we conclude that the results for the double differential cross-sections using the low-density parametrization and the self-consistently calculated width are almost the same due to the comparable widths (see figures 5.2, 5.3 and 5.4).

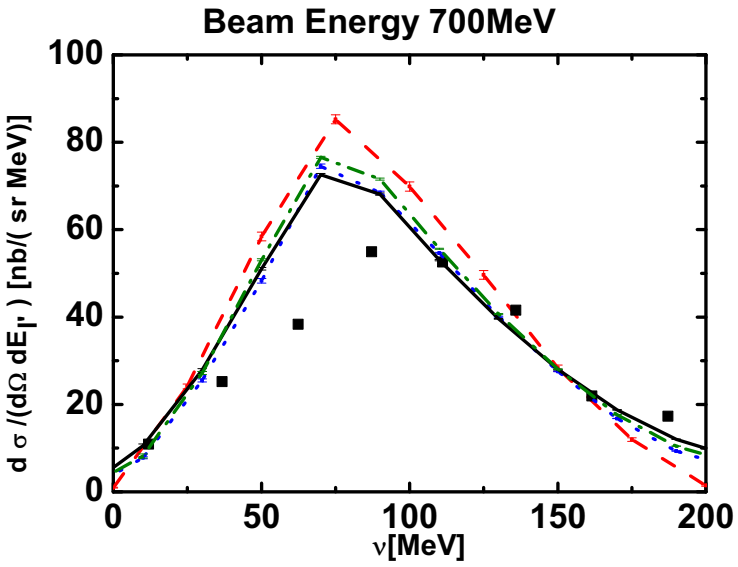

Figure 5.2: Electron induced inclusive double differential cross section for $e^- + {}^{16}_{8}\mathrm{O} \rightarrow e^- + X$ as a function of the energy transfer ν at fixed outgoing electron angle of $\theta = 32°$. The dashed line shows the result using a sharp particle for the outgoing nucleon ($\Gamma = 1$ MeV for numerical reasons) and a Fermi step function in the LDA, the dotted curve the result of the calculation performed with the low density width parametrization (5.13) and a Fermi step function in the LDA, the dash-dotted line the result of the calculation using the self-consistently calculated width of chapter 2 and a Fermi step function in the LDA, the black solid line the result of the calculation using the self-consistently calculated width of chapter 2 and the parametrization of the momentum distribution of chapter 4, the black squares the experimental data measured on oxygen at the ADONE storage ring [A$^+$96].

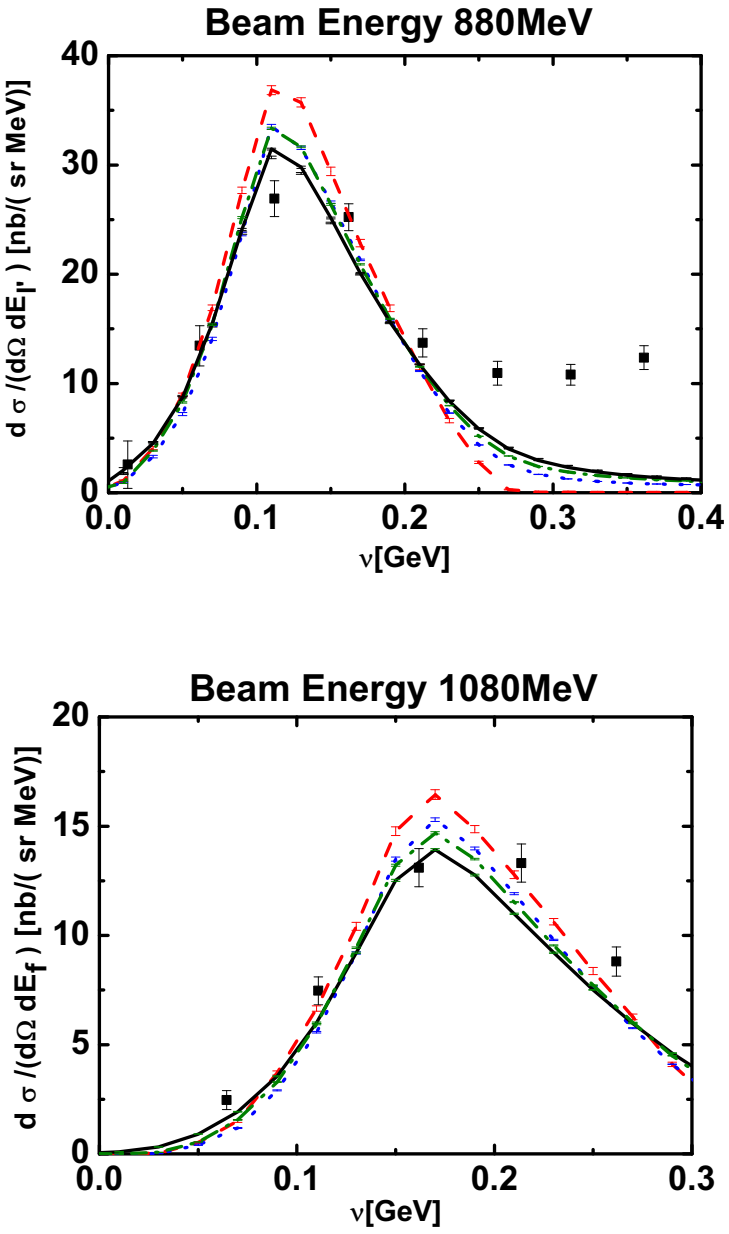

Figure 5.3: Same as figure 5.2 for 880 MeV and 1080 MeV beam energies

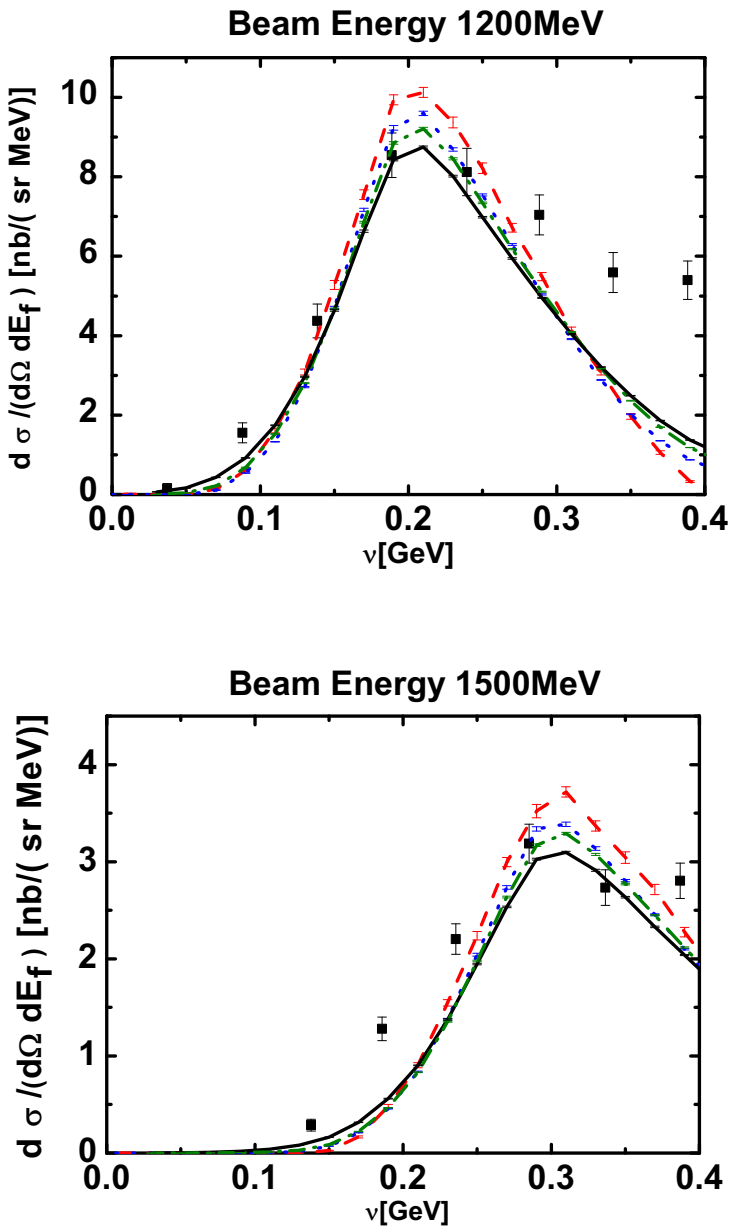

Figure 5.4: Same as figure 5.2 for 1200 MeV and 1500 MeV beam energies

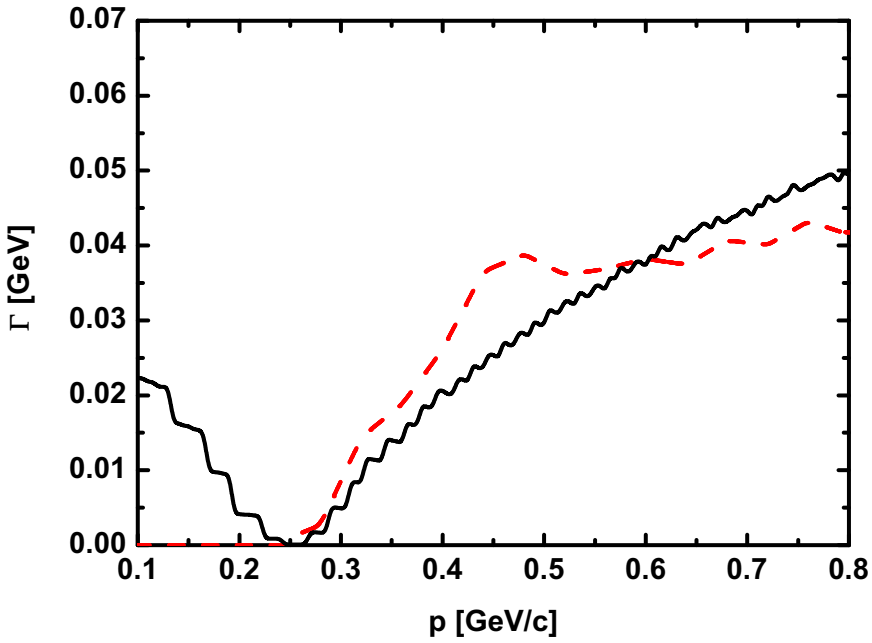

Figure 5.5: Comparison of the on-shell width as a function of the momentum for the density $\rho = -0.16$ fm^{-3}: The dashed line shows the on-shell width for the low-density width parametrization (5.13), the solid line the on-shell width for the self-consistently calculated width of chapter 2.

5.6 Results for Neutrino Induced Quasi Elastic Scattering

Now we want to calculate neutrino induced scattering processes. We are interested in the inclusive cross section for neutrino scattering on nuclei. Figure 5.6 shows the quasi elastic contribution to the inclusive cross section per nucleon of the process

$$\nu_\mu + \ {}^{16}_{8}\mathrm{O} \rightarrow \mu^- + X$$

as a function of the muon energy E_μ at fixed incoming neutrino energy of 0.7 GeV and fixed outgoing muon angle of $\theta = 20°$. Since the electron data that we used for the electron induces reaction was measured on ${}^{16}_{8}\mathrm{O}$ we use the same target for the neutrino induced reactions. We have performed several calculations on different levels of optimization. The first calculation (dashed line) is done with a Fermi step function in nuclear matter, but using the local density approximation (LDA), and a sharp particle ($\Gamma = 1$ MeV for numerical reasons) as outgoing nucleon. The quasi-elastic peak is at about $E_\mu = 0.66$ GeV with an amplitude of $10.25 \cdot 10^{-38}\ cm^2/$ GeV which, using the electron data in section 5.5 as a benchmark, is considered to be too high.

The dotted line shows the calculation performed with the low density approximation (5.13) and with a Fermi step function in nuclear matter, but with LDA. We observe a decrease of the quasi elastic peak to $9.29 \cdot 10^{-38}\ cm^2/$ GeV. Furthermore, we observe an increase in the cross section between $E_\mu = 0.45$ GeV and $E_\mu = 0.6$ GeV compared to the previous result (dashed line). This is due to the fact that the collision width (5.13) includes nucleon-nucleon collisions.

The next calculation (dash-dotted line) was done with the self-consistently calculated width in chapter 2 and with a Fermi step function in nuclear matter, but with LDA. We see that the quasi elastic peak further decreases. Furthermore, we observe an increase in the cross section between $E_\mu = 0.45$ GeV and $E_\mu = 0.6$ GeV compared to the two previous calculations (dashed line and dotted line). This is due to the fact that the self-consistently calculated width includes in second order short range nucleon-nucleon interactions, e.g. two-particle one-hole excitations or one-particle two-hole excitations, so that the calculation includes collisions with more than one nucleon.

The final calculation (solid line) was performed with the modification of the initial nucleon from section 4.1.1 and the width from chapter 2 . We see that the quasi elastic peak decreases to $8.45 \cdot 10^{-38}\ cm^2/$ GeV. The broadening between $E_\mu = 0.45$ GeV and $E_\mu = 0.6$ GeV is higher than in the case of a step function (dash-dotted line). However, the difference can become bigger if one initializes the particles according to the spectral function because that would increase the number of off-shell particles in the initial nucleus.

In chapter 4 we introduced two parametrizations. One is fitted to the momentum distribution of Lehr [Leh03] the other is fitted to the momentum distribution of our self-consistent calculation. Figure 5.7 shows the inclusive cross section for the same process as before The dashed line shows the result of the calculation performed with the self-consistently calculated width of chapter 2 and the parametrization of the momentum distribution of chapter 4, using the parameters fitted to the momentum distribution by Lehr [Leh03]. The red dotted line shows the result of the calculation performed with the self-consistently calculated width of chapter 2 and the parametrization of the momentum distribution of section 4.1.1 using the parameters for our momentum distribution of chapter 3. We see that the difference between these two parametrization is very small. Except this calculations all calculations are performed with the parameters fitted to Lehr. However, the difference can become bigger if one initialize the nucleus with the full spectral function.

Since there are no neutrino data available we compare our calculations with sophisticated theoretical calculations from Benhar et al. [BM06]. We use the calculations of Benhar as reference because their nuclear many-body theory (NMBT) calculation of the spectral function. This allows us to examine how good our "simple" model is.

Figure 5.8 shows the total inclusive cross section for

$$\nu_e + {}^{16}_{8}\mathrm{O} \rightarrow e^- + X$$

as a function of the neutrino energy from $E_\nu = 0$ GeV to 1.4 GeV. The dash-dot-dotted curve shows eight times the vacuum process, the reaction happens only on neutrons due to charge conservation. The cross section starts at zero at zero neutrino energy because we need at least 0.511 MeV in order to create an electron. The function rises at energies from 0.1 GeV to 1.0 GeV before it reaches its saturation value of $\sigma = 0.55 \cdot 10^{-38}\ cm^2$.

The dashed curve shows the calculation from Benhar et al. [BM06] for a relativistic Fermi gas model without Pauli blocking (RFGM-NoPB). This calculations assumes a delta-functions for the nucleons. We see that the total cross section decreases. For saturation the total cross section is $\sigma = 0.53 \cdot 10^{-38}\ cm^2$.

The dotted curve shows the calculation from Benhar with the NMBT spectral function but without Pauli blocking (SF-NoPB). The total cross section is further reduced, in particular in the rising region between $E_\nu = 0 - 0.8$ GeV.

The lower dash dotted curve shows the calculation with the spectral function and with Pauli blocking (SF-PB) from Benhar. We can see that Pauli blocking has no big effect in the rising region but it reduces the saturation value of the total cross section to $\sigma = 0.48 \cdot 10^{-38}\ cm^2$.

Let us now consider the self-consistently calculated width from chapter 2. The solid black line shows the GiBUU calculation including the self-consistently calculated width, Pauli blocking, the momentum dependent mean field and the modification of the nucleon momentum distribution of chapter 4. We see that the

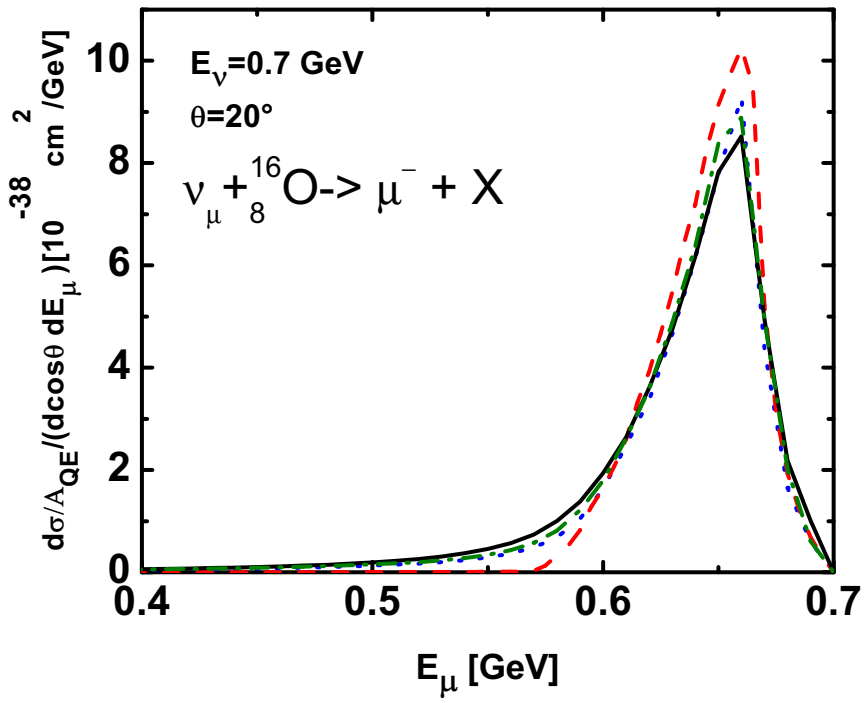

Figure 5.6: Inclusive cross section of the process $\nu_\mu + {}^{16}_{8}O \to \mu^- + X$ at fixed incoming neutrino energy of 0.7 GeV and fixed outgoing muon angle of $\theta = 20°$. The dashed line shows the result calculated with a constant width of 1 MeV and a Fermi step function in the LDA, the dotted line shows the result using the low density parametrization (5.13) and a Fermi step function in the LDA, the dash-dotted line shows the result using the self-consistently calculated width of chapter 2 and a Fermi step function in the LDA and the black solid line shows the result using the self-consistently calculated width of chapter 2 and the parametrization of the momentum distribution of chapter 4.

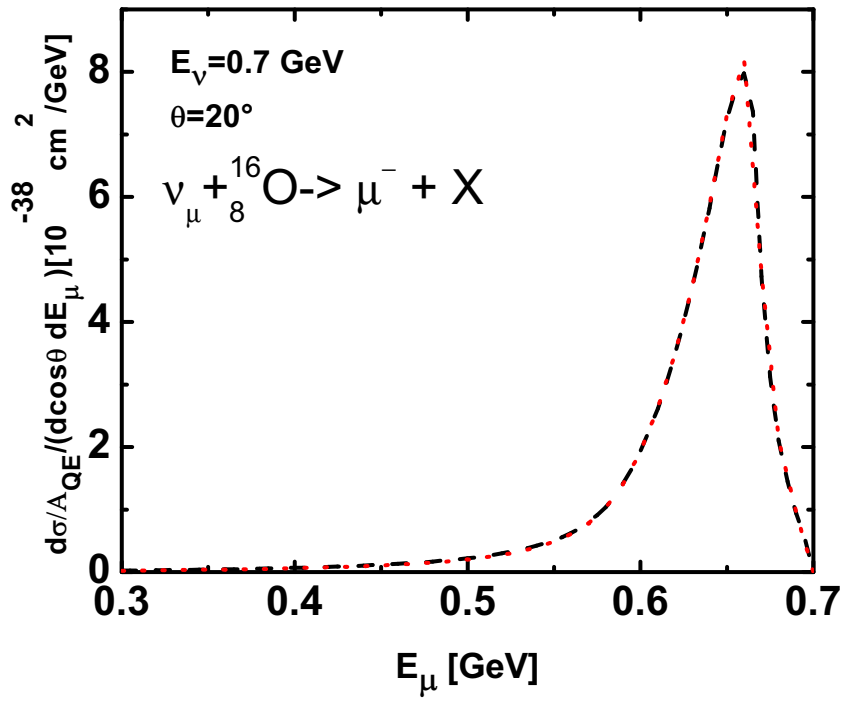

Figure 5.7: Same as figure 5.6. The black dashed line shows the result of the calculation performed with the self-consistently calculated width of chapter 2 and the parametrization of the momentum distribution of chapter 4, using the parameters fitted to the momentum distribution of Lehr [Leh03]. The dotted line shows the result of the calculation performed with the parameters for the momentum distribution of chapter 3.

result corresponds to the results of the most realistic calculation from Benhar et al. [BM06] (lower dash dotted curve). We conclude that our model describes the nucleon-nucleon correlations as good as the more sophisticated model of Benhar et al. Since all information of the energy and momentum distribution of the outgoing particle are "integrated out" in the total cross section it will be interesting to calculate exclusive cross section in the future.

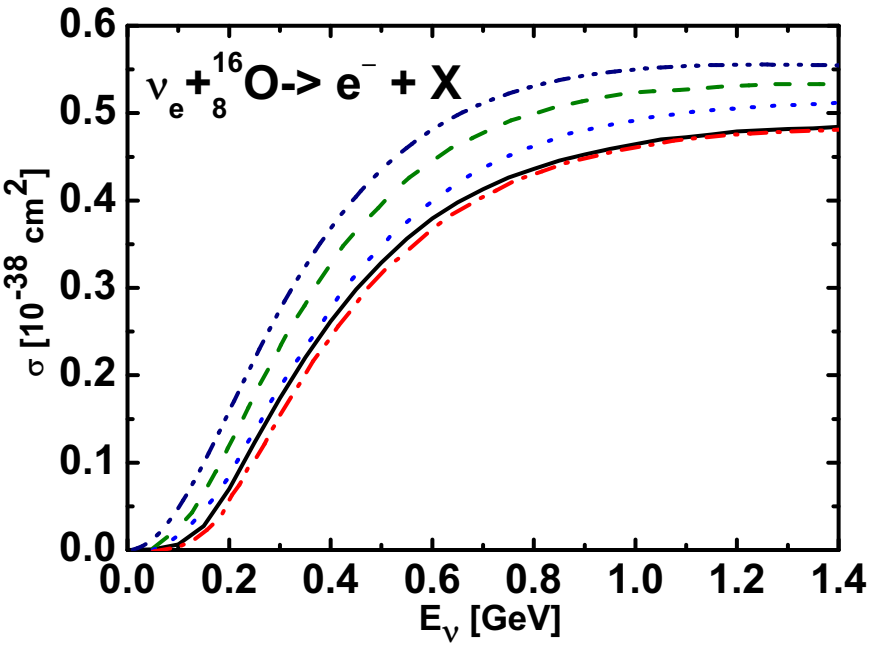

Figure 5.8: A comparison of our results for the total quasi elastic cross section for the process $\nu_e + {}^{16}_{8}\mathrm{O} \rightarrow e^- + X$ as a function of the incoming neutrino energy E_ν to calculations from Benhar et al. [BM06]: The black solid line shows the result of our calculation performed with the self-consistently calculated width of chapter 2 and the parametrization of the momentum distribution of chapter 4, the dash-dot-dotted curve eight times the vacuum process, the dashed curve the calculation from Benhar for a relativistic Fermi gas model without Pauli blocking (RFGM-NoPB), the dotted curve the calculation from Benhar with the spectral function but without Pauli blocking (SF-NoPB), dash dotted curve the calculation with the spectral function and with Pauli blocking (SF-PB) from Benhar.

6 Summary and Outlook

In this work we have examined the influence of in-medium modifications on the quasi-elastic scattering of electrons and neutrinos on nuclei. Motivated by electron-nucleus scattering experiments [A$^+$96] and sophisticated calculations performed by Benhar et al. [BFN$^+$05] we have implemented short-range nucleon-nucleon correlations in the GiBUU model. Moreover, we have improved the ground state of the nucleus by replacing the Fermi gas by a more realistic distribution. The calculations have shown that the results with our improvements match the data of [A$^+$96] for low momentum transfer better than the calculations without these modifications. Moreover, our calculations for the neutrino-nucleus total cross section correspond to the nuclear many-body theory (NMBT) calculations from Benhar et al. [BM06].

We have seen that the mean field approximation acts like an external potential. Hence, the particles can still be treated like free particles. Including the second order collision terms in the self-consistently calculated self-energy yields an imaginary part for the self-energy such that the quasi-particle peak is broadened to a resonance with a finite lifetime. With a constant matrix element, i.e. a pointlike interaction in coordinate space, the collision terms take into account short-range nucleon-nucleon correlations. Thus, we obtain a momentum distribution that contains occupied states above the Fermi momentum. Due to the smaller phase space, the width below the Fermi energy is much smaller than the width above the Fermi energy. Moreover, we have observed a linear density dependence of the self-consistently calculated width for densities up to $\rho = 0.8$ fm^{-3}. For higher densities, we have observed a saturation of the width above the Fermi energy. Thus, a constant scaling factor for the width cannot be applied anymore.

We have improved the initialization of the nucleons in the nuclei of the GiBUU model by including the high-momentum tail of the momentum distribution. Furthermore, we have shown how the width between two density grid points can be interpolated such that the width is always zero at the local Fermi energy.

Using the self-consistently calculated width, which includes short-range nucleon-nucleon correlations, reduces the height of the quasi-elastic peak of the electron-nucleus scattering and broadens it. Hence, at low momentum transfer short-range nucleon-nucleon correlations have an influence on the inclusive double differential quasi-elastic cross section. Thus, the two-particle one-hole excitations and the one-particle two-hole excitations that are included in the self-consistently calculated width improve the description of the nucleons in our model. In particular, the calculations with short-range correlations match the electron scattering data

on oxygen [A$^+$96] at low energy transfer better than the calculations without these modifications. Furthermore, we have seen that the influence of the high-momentum tail, that comes from the broadening of the spectral function and populates states with higher momenta than the Fermi momentum, on the results is of the same order as the implementation of the self-consistently calculated width for the outgoing particle in the elementary cross section. For higher beam energies we have seen that the short-range correlations play a minor role because of the higher energy transfer at the quasi-elastic peak.

Using the low-density approximation for the width in our model yields almost the same results as using the self-consistently calculated width. We can conclude that the inclusive cross section is not sensitive to the particular shape of the spectral function but is sensitive to the reduction of the strength inside the kinematical integration limits.

For the neutrino-nucleus scattering, our results with the self-consistently calculated width correspond to the "state of the art" calculation from Benhar et al. [BM06]. We can conclude that our simpler model describes the nucleon-nucleon correlations as well as the approach of Benhar et al.

In further examinations it will be crucial to check in exclusive reactions whether a calculation using the spectral functions can describe experimental data or not. To do so we have to propagate off shell nucleons through nuclei. For that purpose we should determine the width in a self-consistent calculation with the same mean field as in the GiBUU model. Moreover, we could improve the self-consistent calculation by introducing a density dependent matrix element.

The recent results are encouraging that this simple model can indeed describe the short-range nucleon-nucleon correlation effects for low momentum transfer. For the future it will be interesting to see how good this model works for other reactions and cross sections.

A Convention

A.1 Natural Units

In this thesis we used the so called natural units with

$$\hbar = c = 1 \ . \tag{A.1}$$

For all masses and energies we use GeV as standard unit. In general GeV is also used for the momentum but to distinguish between the spacial momentum and the energy we indicate the momentum with GeV/c. The dimension of mass, length and time are:

$$[M] = [L]^{-1} = [T]^{-1} \ . \tag{A.2}$$

For the conversion into SI-units we use the formula

$$\hbar c = 0.197 \text{ GeVfm} \ . \tag{A.3}$$

A.2 Dirac Matrices

Throughout this thesis we use the conventions from [BD]. The metric tensor is given by

$$g^{\mu\nu} = \begin{pmatrix} 1 & 0 & 0 & 0 \\ 0 & -1 & 0 & 0 \\ 0 & 0 & -1 & 0 \\ 0 & 0 & 0 & -1 \end{pmatrix} \ . \tag{A.4}$$

For the Dirac matrices we use the following representation:

$$\begin{aligned} \gamma^\mu &= (\gamma^0, \vec{\gamma}) \\ \gamma^0 &= \gamma_0 = \begin{pmatrix} \mathbb{1} & 0 \\ 0 & -\mathbb{1} \end{pmatrix} \ , \\ \vec{\gamma} &= \begin{pmatrix} 0 & \vec{\sigma} \\ -\vec{\sigma} & 0 \end{pmatrix} , \end{aligned}$$

with the 2×2 unit matrix $\mathbb{1}$ and the Pauli spin matrices

$$\begin{aligned} \vec{\sigma} &= (\sigma_1, \sigma_2, \sigma_3) \ , \\ \sigma_1 &= \begin{pmatrix} 0 & 1 \\ 1 & 0 \end{pmatrix} \ , \\ \sigma_2 &= \begin{pmatrix} 0 & -i \\ i & 0 \end{pmatrix} \ , \\ \sigma_3 &= \begin{pmatrix} 1 & 0 \\ 0 & -1 \end{pmatrix} \ . \end{aligned}$$

Furthermore we need the following combinations of those matrices:

$$\gamma_5 = \gamma^5 = i\gamma^0\gamma^1\gamma^2\gamma^3 = \begin{pmatrix} 0 & \mathbb{1} \\ \mathbb{1} & 0 \end{pmatrix} \ ,$$
$$\sigma^{\mu\nu} = \frac{i}{2}[\gamma^\mu, \gamma^\nu] \ .$$

We use the totally antisymmetric tensor $\epsilon_{\alpha\beta\gamma\delta}$ with the convention $\epsilon_{0123} = 1$.

B Mandelstam Variables

The differential cross section for a scattering process with two particles in the initial state and n particles in the finals state is given by

$$d\sigma = \frac{(2\pi)^4 |\mathcal{M}|^2}{4\sqrt{(p_1 \cdot p_2) - m_1^2 m_2^2}} \times d\Phi_n(p_1 + p_2; p_3, \ldots, p_{n+2}) \ , \tag{B.1}$$

where $d\Phi_n$ is an element of the n-body phase space given by

$$d\Phi_n(p_1 + p_2; p_3, \ldots, p_n + 2) = \delta^4(p_1 + p_2 - \sum_{i=2}^{n+2} p_i) \prod_{i=3}^{n+2} \frac{d^4 p_i}{(2\pi)^4} \delta(p^2 - M_i^2) \ . \tag{B.2}$$

For two-body reactions we use the Lorentz-invariant Mandelstam variables shown s, t, u. The variable s is the square of the center of mass energy, the Mandelstam variable t is the square of the transfered momentum and u only appears for identical particles in the final state (see figure B.1)

$$\begin{aligned} s &= (p_1 + p_2)^2 = (p_3 + p_4)^2 \\ &= m_1^2 + 2E_1 E_2 - 2\vec{p}_1 \cdot \vec{p}_2 + m_2^2 \\ t &= (p_1 - p_3)^2 = (p_2 - p_4)^2 \\ &= m_1^2 - 2E_1 E_3 - 2\vec{p}_1 \cdot \vec{p}_3 + m_3^2 \\ u &= (p_1 - p_4)^2 = (p_2 - p_3)^2 \\ &= m_1^2 - 2E_1 E_4 - 2\vec{p}_1 \cdot \vec{p}_4 + m_4^2 \ . \end{aligned}$$

They satisfy the equation

$$s + t + u = m_1^2 + m_2^2 + m_3^2 + m_4^2 \ .$$

The Mandelstam variables are physical quantities and therefore it is useful to express the cross sections through these quantities. Consider a two-particle collision with identical particles in the final state. At tree level where there are no virtual momenta loops, we have three kinematic scenarios (see figure B.1).

With the Mandelstam variables we can write the two-body cross section as

$$\frac{d\sigma}{dt} = \frac{1}{64\pi s} \frac{1}{|p_{1cm}|^2} \ |\mathcal{M}|^2 \ .$$

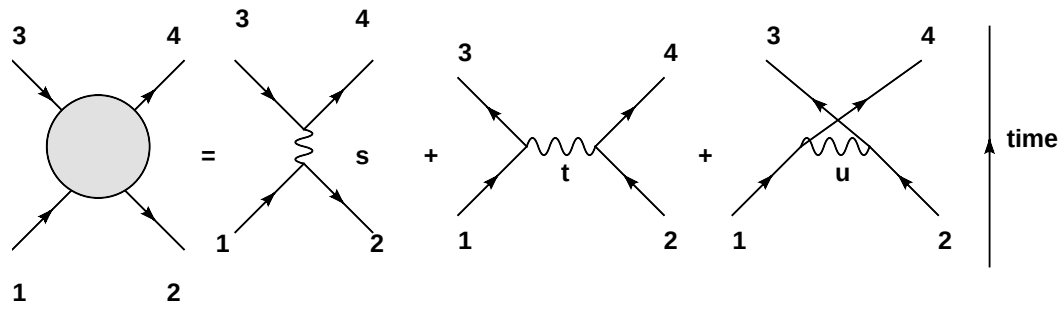

Figure B.1: physical interpretation of the Mandelstam variables.

C Substitution

In some cases we have to integrate over the on-shell peak of the spectral function. Since this peak is narrow compared to the integration volume we "reshape"' the spectral function. Let us consider the integral

$$I(\omega) = \int_{p_{min}}^{p_{max}} dp p^2 A(\omega,p) f(\omega,p) = \int_{p^2_{min}}^{p^2_{max}} dp^2 \frac{p}{2} A(\omega,p) f(\omega,p) \ , \quad \text{(C.1)}$$

with $\mathcal{A}(\omega,p)$ the spectral function

$$\mathcal{A}(\omega,\vec{p}) = \frac{\Gamma(\omega,\vec{p})}{(\omega - \frac{p^2}{2m} - U)^2 + \frac{\Gamma(\omega,\vec{p})^2}{4}} \quad \text{(C.2)}$$

and am arbitrary function $f(\omega,p)$. The on-shell condition is given by

$$\omega - \frac{p^2}{2m} - U = 0 \ . \quad \text{(C.3)}$$

A substitution $p^2 \to y$ should either spread out the on-shell region, so that the numerical integration is possible, or generate a factor $\frac{dp^2}{dy}$ that compensates the peak structure of the spectral function. The substitution

$$y(\omega) = 2 \arctan\left(\frac{2}{\Gamma}(\omega - \frac{p^2}{2m} - U)\right) \quad \text{(C.4)}$$

has both features. It is inspired by the denominator of the spectral function and $\frac{d\arctan(x)}{dx} = (1+x^2)^{-1}$. The derivative is

$$\frac{dy}{dp^2} = \frac{-\Gamma}{2m} \frac{1}{(\omega - \frac{p^2}{2m} - U)^2 + \frac{\Gamma^2}{4}} \ . \quad \text{(C.5)}$$

Inserting (C.5) in (C.1) cancels the denominator (exactly for a constant width) of the spectral function:

$$\begin{aligned} I(\omega) &= \frac{1}{2} \int_{y(\omega,p_{min})}^{y(\omega,p_{max})} dy \frac{dp^2}{dy} p(y) A(\omega,p(y)) f(\omega,p(y)) \\ &= -m \int_{y(\omega,p_{min})}^{y(\omega,p_{max})} dy \ p(y) f(\omega,p(y)) \ . \end{aligned} \quad \text{(C.6)}$$

In our calculations we are dealing with an energy and momentum dependent width and potential. However, the width and the potential do not change as fast as the spectral function at the on-shell peak. Therefore, we can use the width of the on-shell peak and the corresponding potential, including the real part of the self energy, in the substitution (C.5). Thus, the on-shell peak is broadened and can be integrated numerically.

D Properties of $\Sigma^<$ and $\Sigma^>$

D.1 Energy Properties

Replacing the Green's functions in (2.62) and (2.63) by the distribution function and the spectral function yields

$$\begin{aligned}\Sigma^>(\omega,\vec{p}) &= \int \ldots \delta(\vec{p}+\vec{p}_2-\vec{p}_3-\vec{p}_4)\delta(\omega+\omega_2-\omega_3-\omega_4) \\ &\quad \times \mathcal{A}(\omega_2,\vec{p}_2)\mathcal{A}(\omega_3,\vec{p}_3)\mathcal{A}(\omega_4,\vec{p}_4)n(\omega_2,\vec{p}_2)[1-n(\omega_3,\vec{p}_3)][1-n(\omega_4,\vec{p}_4)] \ ,\end{aligned} \tag{D.1}$$

and

$$\begin{aligned}\Sigma^<(\omega,\vec{p}) &= \int \ldots \delta(\vec{p}+\vec{p}_2-\vec{p}_3-\vec{p}_4)\delta(\omega+\omega_2-\omega_3-\omega_4) \\ &\quad \times \mathcal{A}(\omega_2,\vec{p}_2)\mathcal{A}(\omega_3,\vec{p}_3)\mathcal{A}(\omega_4,\vec{p}_4)[1-n(\omega_2,\vec{p}_2)]n(\omega_3,\vec{p}_3)n(\omega_4,\vec{p}_4) \ .\end{aligned} \tag{D.2}$$

The functions $n(\omega_i,\vec{p}_i)$ ensure that only states contribute that are occupied, while the $[1-n(\omega_i,\vec{p}_i)]$ functions ensure that final states are unoccupied. The δ-function demands

$$\omega+\omega_2=\omega_3+\omega_4 \ .$$

We assume that the Fermi distribution is a step function. For $\Sigma^>(\omega,p)\neq 0$ we need $\omega_2<\omega_F$, $\omega_3>\omega_F$ and $\omega_4>\omega_F$. These constraints lead to the lower limit

$$\omega=\omega_3+\omega_4-\omega_2>2\omega_F-\omega_F=\omega_F \ .$$

An energy of at least $2\omega_F$ is required for the two unoccupied states. Since ω_2 is determined by $n(\omega_2,p_2)$ we cannot have an energy above ω_F. Hence, ω has to be at least ω_F.

For $\Sigma^<(\omega,p)\neq 0$ we have the opposite constraints. These lead to

$$\omega=\omega_3+\omega_4-\omega_2<2\omega_F-\omega_F=\omega_F \ .$$

The total energy of the two occupied states is lower than $2\omega_F$. The energy of ω_2 has to be at least ω_F. Thus, the energy ω cannot be above ω_F.

If the distribution function is not a step function these constraints will not be strict. However, the dominance of $\Sigma^<$ below the Fermi energy and the dominance $\Sigma^>$ above the Fermi energy remain.

D.2 Momentum Properties

For the momentum properties we have to take a closer look at the equations (D.1) and (D.2). We see that these equations measure the overlap of the spectral functions $\mathcal{A}(\omega_2, \vec{p}_2)$, $\mathcal{A}(\omega_3, \vec{p}_3)$ and $\mathcal{A}(\omega_4, \vec{p}_4)$ in their integration limits. The momentum δ-function demands

$$\vec{p} = \vec{p}_3 + \vec{p}_4 - \vec{p}_2 \ .$$

We assume again that the Fermi distribution is a step function. For $\Sigma^<(\omega, p)$ the momenta are restricted to $|\vec{p}_2| > p_F$, $|\vec{p}_3| < p_F$ and $|\vec{p}_4| < p_F$. The momenta $\vec{p}_2$, $\vec{p}_3$ and $\vec{p}_4$ determine the poles of the spectral functions. Hence, the overlap of the spectral functions is big for momenta that are close together. Furthermore, the phase space of the equations (D.1) and (D.2) reaches its maximum for equal distributed momenta. The momentum $\vec{p}_3 + \vec{p}_4$ has its maximum for parallel momenta and $|\vec{p}_3| = |\vec{p}_4| = p_F$. Therefore, a high momentum $\vec{p}$, compared to the Fermi momentum, has to be compensated by the momentum $\vec{p}_2$. Thus, the pole of $\mathcal{A}(\omega_2, \vec{p}_2)$ is far away from the spectral functions $\mathcal{A}(\omega_3, \vec{p}_3)$ and $\mathcal{A}(\omega_4, \vec{p}_4)$ so that the overlap decreases and $\Sigma^<(\omega, p)$ decreases for high momenta.

For $\Sigma^>(\omega, p)$ the momenta are restricted to $|\vec{p}_2| < p_F$, $|\vec{p}_3| > p_F$ and $|\vec{p}_4| > p_F$. In this case $|\vec{p}_2| < p_F$ and therefore $\Sigma^>(\omega, p)$ decreases for high momenta too.

Bibliography

[A+96] M. Anghinolfi et al., *Quasi-elastic and inelastic inclusive electron scattering from an oxygen jet target*, Nucl. Phys. **A602** (1996) 405, `nucl-th/9603001`.

[AGD63] A. Abrikosov, L. Gorkov, and I. Dzyaloshinski, *Methods of Quantum Field Theory in Statistical Physics*, Dover Publications, 1963, ISBN 0-46863228-8.

[BARLM07] O. Buss, L. Alvarez-Ruso, A. B. Larionov, and U. Mosel, *Exciting pions in nuclei: DCX and electroproduction in the resonance region* (2007), `nucl-th/0703060`.

[BBA03] H. Budd, A. Bodek, and J. Arrington, *Modeling quasi-elastic form factors for electron and neutrino scattering* (2003), `hep-ex/0308005`.

[BBBA06] R. Bradford, A. Bodek, H. Budd, and J. Arrington, *A new parameterization of the nucleon elastic form factors*, Nucl. Phys. Proc. Suppl. **159** (2006) 127, `hep-ex/0602017`.

[BBG+92] M. Baldo, I. Bombaci, G. Giansiracusa, U. Lombardo, C. Mahaux, and R. Sartor, *Off-the-energy-shell properties of the mass operator and spectral functions in nuclear matter*, Nucl. Phys. **A545** (1992) 741.

[BD] J. D. Bjorken and S. D. Drell, *Relativistic Quantum Field Theory. (German Translation)*, bibliograph.Inst./Mannheim 1967, 409 P.(B.i.- Hochschultaschenbuecher, Band 101).

[BFF89] O. Benhar, A. Fabrocini, and S. Fantoni, *The nucleon spectral function in nuclear matter*, Nucl. Phys. **A505** (1989) 267.

[BFF92] O. Benhar, A. Fabrocini, and S. Fantoni, *Nuclear-matter green functions in correlated-basis theory*, Nucl. Phys. **A550** (1992) 201.

[BFN+05] O. Benhar, N. Farina, H. Nakamura, M. Sakuda, and R. Seki, *Electron and neutrino nucleus scattering in the impulse approximation regime*, Phys. Rev. **D72** (2005) 053005, `hep-ph/0506116`.

[BGPR96] S. Boffi, C. Giusti, F. D. Pacat, and M. Radici, *Electromagnetic Response of Atomic Nuclei*, Oxford University Press, 1996, ISBN 0 19 851774 2.

[BLARM07] O. Buss, T. Leitner, L. Alvarez-Ruso, and U. Mosel, *The influence of the nuclear medium on inclusive electron and neutrino scattering off nuclei* (2007), `arXiv:0707.0232[nucl-th]`.

[BM06] O. Benhar and D. Meloni, *Total neutrino and antineutrino nuclear cross sections around 1 gev* (2006), `hep-ph/0610403`.

[Bro] L. S. Brown, *Quantum field theory* Cambridge, UK: Univ. Pr. 1992 542 p.

[CMB+97] E. Chabanat, J. Meyer, P. Bonche, R. Schaeffer, and P. Haensel, *A skyrme parametrization from subnuclear to neutron star densities*, Nucl. Phys. **A627** (1997) 710.

[Dan84] P. Danielewicz, *Quantum theory of nonequilibrium processes. 1*, Annals Phys. **152** (1984) 239.

[DB04] W. H. Dickhoff and C. Barbieri, *Self-consistent green's function method for nuclei and nuclear matter*, Prog. Part. Nucl. Phys. **52** (2004) 377, `nucl-th/0402034`.

[DF83] T. De Forest, *Off-shell electron nucleon cross-sections. the impulse approximation*, Nucl. Phys. **A392** (1983) 232.

[Dic05] W. H. Dickhoff, *Many Body Theory Exposed!*, World Scientific, 2005, ISBN 981-256-294-X.

[FLM03] F. Froemel, H. Lenske, and U. Mosel, *Short-range correlations in nuclear matter at finite temperatures and high densities*, Nucl. Phys. **A723** (2003) 544, `nucl-th/0301038`.

[Fro01] F. Froemel, *Selbstkonsistente Berechnung der Quark-Spektralfunktion in unendlich ausgedehnter Quarkmaterie*, Diplomarbeit, Institut für Theoretische Physik, Justus-Liebig-Universität Giessen, 2001, URL `theorie.physik.uni-giessen.de/html/publications.html`.

[FW71] Fetter and Walecka, *Quantum Theory of Many-Body Systems*, McGraw-Hill Inc., 1971.

[GiB] *GiBUU Project* ***http://gibuu.physik.uni-giessen.de/GiBUU***.

[GWP+90] C. Gale, G. Welke, M. Prakash, S. L. S., and D. Gupta, *Transverse momenta, nuclear equation of state, and momentum-dependent interactions in heavy-ion collisions*, Phys. Rev. C **41** (1990).

[KB62] L. Kadanoff and G. Baym, *Quantum Statistical Mechanics*, W.A. Benjamin, Inc., 1962.

[KLM05] P. Konrad, H. Lenske, and U. Mosel, *Short range correlations and spectral functions in asymmetric nuclear matter*, Nucl. Phys. **A756** (2005) 192, `nucl-th/0501007`.

[Kon04] P. Konrad, *Kurzreichweitige Korrelationen in asymmetrischer Kernmaterie*, Diplomarbeit, Institut für Theoretische Physik, Justus-Liebig-Universität Giessen, 2004, URL `theorie.physik.uni-giessen.de/html/publications.html`.

[Leh57] H. Lehmann, *Über Eigenschaften von Ausbreitungsfunktionen und Renormierungskonstanten quantisierter Felder* , Nuovo Cimento **11** (1957) 342.

[Leh03] J. Lehr, *In-Medium-Eigenschaften von Nukleonen und Nukleonresonanzen in einem semiklassischen Transportmodell*, Doktorarbeit, Institut für Theoretische Physik, Justus-Liebig-Universität Giessen, 2003, URL `theorie.physik.uni-giessen.de/html/publications.html`.

[Min] *MiniBooNE experiment* ***http://www-boone.fnal.gov/***.

[NOGR93] J. Nieves, E. Oset, and C. Garcia-Recio, *A theoretical approach to pionic atoms and the problem of anomalies*, Nucl. Phys. **A554** (1993) 509.

[PS] M. E. Peskin and D. V. Schroeder, *An introduction to quantum field theory* Reading, USA: Addison-Wesley (1995) 842 p.

[Tei99] S. Teis, *Transporttheoretische Beschreibung von relativistischen Schwerionen bei SIS-Energien*, Doktorarbeit, Institut für Theoretische Physik, Justus-Liebig-Universität Giessen, 1999.

[WPKG88] G. Welke, M. Prakash, T. Kuo, and S. D. Gupta, *Azimuthal distributions in heavy ion collisions and the nuclear equation of state*, Phys. Rev. C **38** (1988).

Zusammenfassung

Mehr als 50 Jahre Elektron-Nukleon-Streuexperimente haben gezeigt, dass diese Methode wahrscheinlich die ist Kern- und Nukleoneneigenschaften zu untersuchen. Im Jahr 1955 entdeckten Hofstadter und Mc Allister die endliche Protonausdehnung auf Grund von Abweichungen von der Rosenbluth Formel bei elastischer Elektronenstreuung. Die interne Struktur des Neutrons wurde zuerst von Havens et al. und Fermi und Marshall im Jahr 1947 untersucht. In den Jahren 1951-1952 wurde von Foldy gezeigt, dass das anomale magnetische Moment, postuliert von Pauli im Jahr 1941, eine Rolle bei Elektron-Neutron-Streuung spielt.

Für leichte Kerne und hohe Elektronenenergien kann die Bornnäherung, d.h. Ein-Photon-Austausch zwischen Elektron und Target, angewendet werden [DF83]. Die Elektron-Nukleon-Wechselwirkung kann unterteilt werden in einen Vertex, der das Elektron und das Photon enthält, und in einen Vertex, der das Photon an den nuklearen Strom koppelt. Der erste Vertex ist gut verstanden und ausrechenbar durch die Quantenelektrodynamik (QED). Dagegen ist der zweite Vertex, der den nuklearen Strom enthält, wegen der dynamischen Struktur des Nukleonen und deren Wechselwirkung viel schwieriger zu berechnen.

Deshalb nähert man den nuklearen Strom durch die Summe der Ströme der Nukleonen an, die sogenannte Stoßnäherung. Diese Näherung kann angewendet werden, wenn die Wellenlängen kleiner sind als die typischen Nukleon-Nukleon-Abstände. Rechnungen, die die Stoßnäherung benutzen, beschreiben normalerweise auch die experimentellen Daten für inklusive elastische Elektronstreuung [DF83].

Wir wissen jedoch, dass die Stoßnäherung für größere Wellenlängen zusammenbrechen muss. Streuexperimente an Sauerstoff zeigen einen Abfall des quasielastischen Peaks bei einer Elektronenstrahlenergie von 700 MeV [A$^+$96]. Rechnungen von Benhar et al., die eine aus der NMBT (nuclear many-body theory) berechneten Spektralfunktion enthalten, können diese Reduktion des quasielastischen Peaks beschreiben [BFN$^+$05]. Dies zeigt, dass das "freie" Teilchenmodell nicht mehr funktioniert, und dass Nukleon-Nukleon-Korrelationen mit einbezogen werden müssen. Desweiteren haben Neutrino-Experimente an MiniBoone [Min] ein Defizit in Vorwärtsrichtung gemessen, das heutige Modelle nicht beschreiben können.

Am Anfang der vorliegenden Arbeit enthielt das GiBUU [GiB] Transportmodell als In-Medium-Modifikationen ein Fermigasmodell, ein impulsabhängiges Mittelfeld und Pauliblocking in der elementaren Nukleonenreaktion. Das Modell konnte die Elektronstreudaten [A$^+$96] für Strahlenergien höher als 700 MeV

beschreiben. Auch für Energieüberträge oberhalb des quasi-elastischen Peaks beschrieb das Modell die experimentellen Daten, auch bei 700 MeV Strahlenergie.

Motiviert durch die Elektronstreudaten [A$^+$96] und die Berechnungen von Benhar et al. [BFN$^+$05] wurden in der vorliegenden Arbeit in das GiBUU Modell kurzreichweitige Nukleon-Nukleon-Korrelationen implementiert. Außerdem wurde der Grundzustand verbessert indem das Fermigas durch eine realistischere Distribution ersetzt wurde. Die Berechnungen mit diesen Verbesserungen beschreiben die experimentellen Daten [A$^+$96] besser als bisher. Darüber hinaus stimmt die Berechnung für den totalen Neutrino-Nukleus Streuquerschnitt mit der NMBT-Rechnung von Benhar et al. überein.

Die Mittelfeld-Näherung wirkt auf die Teilchen wie ein externes Potential, so dass die Teilchen immer noch als "freie" Teilchen behandelt werden können. Werden jedoch in der selbst-konsistenten Berechnung der Selbstenergien in zweiter Ordnung die Kollisionsterme mit einbezogen, verbreitert sich die Spektralfunktion durch eine endliche Breite. Durch ein konstantes Matrixelement im Impulsraum, das einer Punktwechselwirkung im Ortsraum entspricht, werden kurzreichweitige Nukleon-Nukleon-Korrelationen mit einbezogen. Des Weiteren führt die Verbreiterung der Spektralfunktion zu besetzen Zuständen oberhalb des Fermiimpulses.

Wegen des kleineren Phasenraums sind die Breiten unterhalb der Fermienergie kleiner als oberhalb. Außerdem kann man einen linearen Anstieg der Breite mit der Dichte bis $\rho = 0.8\text{fm}^{-3}$ beobachten. Bei höheren Dichten kann man oberhalb der Fermienergien eine Sättigung erkennen.

Die selbst-konsistenten Breiten reduzieren die Höhe und verbreitern den quasi-elastischen Peak bei den elektroninduzierten inklusiven Streuquerschnitten. Daraus folgt, dass zwei-Teilchen ein-Loch Anregungen und ein-Teilchen zwei-Loch Anregungen, die in der selbst-konsistent berechneten Breite enthalten sind, eine Rolle bei inklusiven Querschnitten bei kleinen Energien spielen. Insbesonders die Rechnungen mit selbstkonsistenter Breite liegen näher an den experimentellen Daten [A$^+$96] als die Rechnungen ohne Berücksichtigung der Breite. Bei höheren Strahlenergien spielen diese Effekte eine kleinere Rolle, da der Energie- und Impulsübertrag am quasi-elastischem Peak größer ist als bei kleineren Strahlenergien. Berechnungen mit der Niedrig-Dichtenäherung [BLARM07] für die Breite ergeben annähernd die selben Resultate wie die Berechnungen mit der selbstkonsistenten Breite.

Die Resultate für den totalen Streuquerschnitt bei der Neutrino-Nukleus-Streuung sind vergleichbar mit den NMBT Berechnungen von Benhar et al. Man kann daraus schließen, dass das Modell den Einfluss der Nukleon-Nukleon-Korrelationen auf die inklusiven quasi-elastischen Streuquerschnitte vergleichbar gut beschreibt wie das anspruchsvollere Modell von Benhar.

In der Zukunft wird es interessant sein zu sehen, ob Rechnungen mit der selbstkonsistenten Breite auch exklusive Reaktionen beschreiben können. Um das zu tun, müssen off-shell Nukleonen durch den Nukleus propagiert werden. Dafür

sollte die selbst-konsistent berechnete Breite mit dem selben Mittelfeld berechnet werden, das in dem GiBUU Modell benutzt wird. Auch der Vergleich inwieweit Rechnungen mit der Niedrig-Dichte-Näherung und Rechnungen mit der selbst-konsistenten Breite bei exklusiven Reaktionen übereinstimmen, wird von Interesse sein. Des Weiteren kann die selbst-konsistente Rechnung durch ein dichteabhängiges Matrixelement verbessert werden.

Die jetzigen Resultate machen zuversichtlich, dass dieses einfache Modell die Nukleon-Nukleon-Korrelationseffekte bei kleinem Impulsübertrag beschreiben kann. In Zukunft wird es interessant sein, inwieweit dieses Modell für andere Prozesse und Streuquerschnitte funktioniert.

Danksagungen

Zuallererst möchte ich Herrn Professor Ulrich Mosel für die Aufnahme in sein Institut danken, sowie dafür, daß er mir die Möglichkeit gegeben hat an einem interresanten und herausfordenden Thema zu arbeiten. Seine vielen Anregungen, Tips und konstruktive Kritik haben mir beim tieferen Verständniss weitergeholfen.

Ganz besonders will ich mich bei Oliver Buß und Tina Leitner bedanken, dass sie mir beim Verständniss der elektron- und neutrino-induzierten Streuquerschnitte geholfen haben und auch für die Durchsicht dieser Diplomarbeit. Auch danke ich dafür, dass sie geduldig alle meine Fragen zu den Geheimnissen des GiBUU codes beantwortet haben. Auch ganz besonderer Dank gilt Patrick Konrad und Frank Frömel, die mir durch zahlreiche Diskussionen beim Verständniss der Nuklearen-Viel-Teilchen-Physik geholfen haben und auch für die Durchsicht dieser Diplomarbeit.

Auch danke ich unserem Administrator Oliver Buss, dass die Cluster und die Rechner keine Probleme gemacht haben.

Meinen Zimmer-Kollegen Fabian Eichstädt, Birger Steinmüller und Stefan Winkelmann danke ich für die gute Atmosphäre und die interessanten physikalischen und nicht physikalischen Gespräche.

Ich danke auch Abdul Ataie und Andreas Fedoseew, die mir einige Kniffe und Tricks bei Fortran gezeigt haben sowie den tollen Editor vi.

Elke Jung danke ich, dass die administrativen Probleme schnell gelöst wurden. Dank ihrer hilfsbereiten Art war der 'Papierkram' immer schnell erledigt.

Allen anderen Mitgliedern des Instituts, die hier nicht namentlich erwähnt sind, danke ich für die nette Atmosphäre.

Meiner Familie danke ich besonders für die Unterstützung während des gesamten Studiums, die sie mir gegeben hat.

Zuletzt will ich noch allen meinen Freunden danken, die mich während des Studiums und darüber hinaus begleitet haben.

Ich versichere hiermit, daß ich diese Diplomarbeit selbstständig verfasst und keine anderen als die angegebenen Quellen und Hilfsmittel benutzt habe.

_____ Gießen, den _____